Force Field for Calcium Sulfate Minerals to Predict Structural, Hydration, and Interfacial Properties

Ratan K. Mishra,[1,2#] Krishan Kanhaiya,[4] Jordan J. Winetrout,[4] Robert J. Flatt[1,3*] and Hendrik Heinz[2,4*]

[1] Department of Civil, Environmental and Geomatic Engineering, ETH Zurich, CH-8093 Zürich, Switzerland

[2] Department of Polymer Engineering, University of Akron, Akron, OH 44325, USA

[3] Sika Technology AG, CH-8048 Zürich, Switzerland

[4] Department of Chemical and Biological Engineering, University of Colorado Boulder, Boulder, CO 80303-0596, USA

[*] Corresponding author: flattr@ethz.ch, hendrik.heinz@colorado.edu

[#] Present address: BASF SE, Materials Molecular Modeling, Carl Bosch Str. 38, 67056 Ludwigshafen, Germany

Abstract

Calcium sulfates such as anhydrite, hemihydrate, and gypsum find widespread use in building materials, implants, and tissue healing. We introduce a simple and compatible atomistic force field for all calcium sulfate phases that reproduces a wide range of experimental data including lattice parameters, surface, hydration, mechanical, and thermal properties in 1% to 5% accuracy relative to experiments. The performance is several times better than prior force fields and DFT methods, which lead to errors in structures and energies up to 100%. We explain (hkl) cleavage energies, the dynamics of (hkl) water interfaces, and new insights into molecular origins of crystal-facet specific hydration and solubility. Impressive agreement of computed and experimentally measured hydration energies is shown. The models add to the Interface force field (IFF) and are compatible with multiple force fields (CHARMM, AMBER, GROMOS, CVFF, PCFF, OPLS-AA) for property predictions of sulfate-containing materials from atoms to the large nanometer scale.

Keywords: calcium sulfate; force field; surface energy; hydration; interfaces

1. Introduction

Gypsum and anhydrite are the most abundant sulfate minerals in the Earth's crust,[1, 2] and calcium sulfates find applications in building materials, medicinal chemistry, energy storage, and geotechnical engineering (Figure 1a).[3, 4] Calcium sulfate minerals are extensively used in building materials such as wallboard due to fire resistance, natural abundance, and low cost.[5, 6] Gypsum also serves as an additive during cement production to regulate the hydration reaction of tricalcium aluminate.[7, 8] In the medical arena, calcium sulfates are used in casts, for bone regeneration, oral surgery, and in guided tissue healing.[3, 9-11] Other uses include geological repositories for radioactive waste, materials for solar energy storage, and geothermal wells.[12-15]

The structural and interfacial properties with electrolyte solutions, the role of organic additives, phase transformations, mechanical and thermal properties play a major role for these applications. However, experimental characterization down to the atomic scale is often not achievable, and understanding of nanoscale properties and interfacial processes requires molecular simulations (Figure 1b).[16-20] Calcium sulfate minerals exist in three major phases: calcium sulfate (anhydrite), $CaSO_4$, calcium sulfate hemihydrate (bassanite or Plaster of Paris), $CaSO_4 \cdot 0.5\ H_2O$, and calcium sulfate dihydrate (gypsum), $CaSO_4 \cdot 2\ H_2O$.[1] Anhydrite and gypsum occur as rock-forming minerals and several partially hydrated phases similar to bassanite are also known.[21, 22] Thermodynamic stability depends on the hydration state, temperature, as well as other environmental conditions. All major phases have the ability to crystallize in the presence of water.[1, 23, 24]

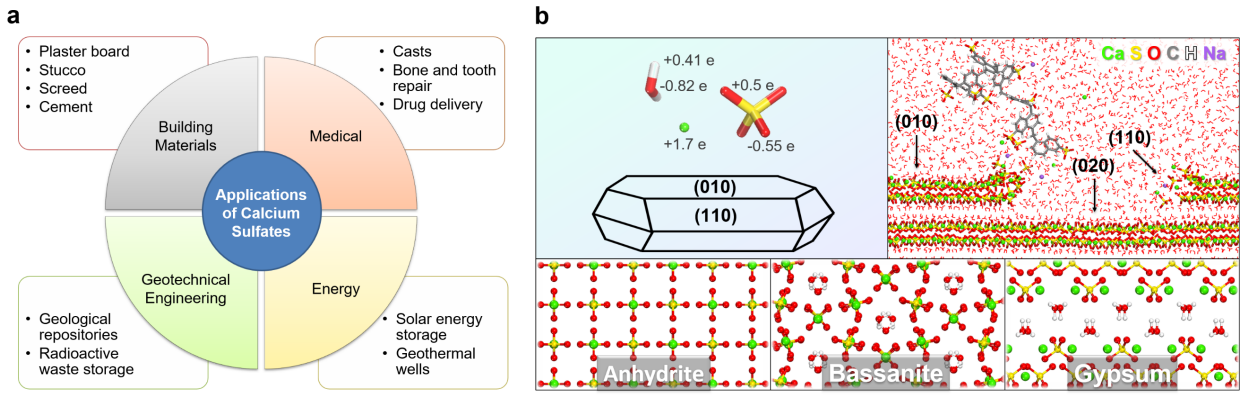

Figure 1. (a) Applications of calcium sulfate mineral phases. (b) Features of the proposed model. All-atom simulations can be used to predict structural, interfacial, and mechanical properties of calcium sulfates and related multiphase materials in high accuracy.

In contrast to nanoscale properties, bulk properties of calcium sulfate minerals have been thoroughly characterized in experiments.[25-44] X-ray diffraction (XRD) data show the common crystal structures, all of which comprise calcium ions, tetrahedral sulfate ions, and, when present, water (Figure 2 and Table S1 in the Supplementary Information).[25-27] Physical and thermodynamic properties are well known.[28-44] Some insights at the molecular level have been obtained using atomic force microscopy (AFM), transmission electron microscopy (TEM), scanning electron microscopy (SEM), nuclear magnetic resonance spectroscopy (NMR), infrared (IR), and Raman spectroscopy.[2, 3, 22, 27, 45-49] However, facet-specific cleavage, hydration and dispersion properties, as well as directional mechanical and thermal properties are barely known due to limitations in visualization and real time imaging. Monitoring of nucleation and growth, interactions with polymers, proteins, DNA, and other minerals at atomic resolution remain largely elusive by current laboratory techniques.

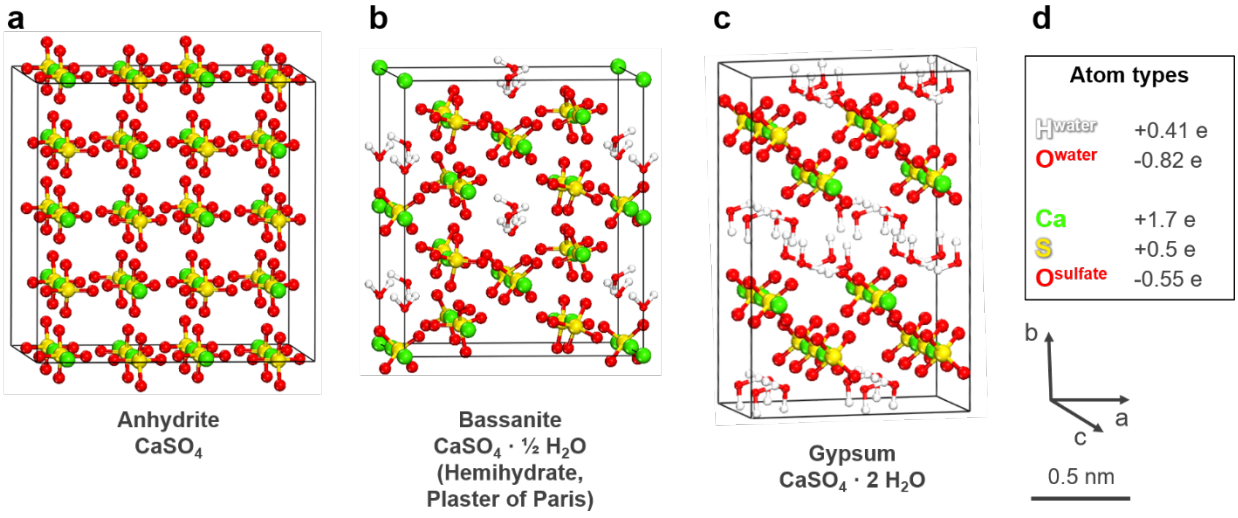

Figure 2. Crystal structures of anhydrite, bassanite, gypsum, as well as atom types and atomic charges for the force field. (a) Orthorhombic β-anhydrite, shown as a (2×2×2) super cell ($a \neq b \neq c$ and $\alpha = \beta = \gamma = 90°$).[26] (b) Monoclinic bassanite, shown as a (1×2×1) super cell ($a \neq b \neq c$ and $\alpha = \gamma \neq \beta$).[25] (c) Monoclinic gypsum, shown as a (2×1×2) super cell.[27, 50] (d) Atom types and atomic charges (in units of e). The atomic charges quantify chemical bonding in the $CaSO_4 \cdot xH_2O$ phases (ref. [51]) and standard water models (SPC, TIP3P, PCFF) can be used without modification.

Molecular simulations for similar minerals (phosphates, silicates) have contributed essential understanding of nucleation and growth, composition-dependent bulk and hydration properties, as well as modification of interfacial properties by organic and polymeric ligands.[17, 52-54] However, there is a chronic lack of reliable models for sulfates. Available models are hardly suitable to perform molecular dynamics simulation of bulk $CaSO_4$ hydrate minerals, electrolyte interfaces, and composite materials with polymers and other minerals. For example, deviations up

to 10% in lattice parameters and overestimates in surface energies up to 150% are found in early models, including computed surface energies of 0.71 J/m^2 for gypsum (010) surfaces[55] versus 0.27 J/m^2 in experiment.[55-57] In addition, earlier Buckingham potentials are incompatible with common models for water and organic molecules, and the performance of these models is similarly low.[58] Generic force fields have been applied to calcium sulfate minerals and tend to be unreliable due to lack of a chemical rationale and validation.[59, 61-64] Major shortcomings are the lack of implementation of a realistic charge distribution,[65] polarizability, and vibrational frequencies. Empirical fits to lattice parameters and mechanical properties without rationale often result in even higher deviations in surface and interfacial energies exceeding 200%. Among more recent models, ReaxFF does not reproduce lattice parameters and surface energies deviate by 100%, and ClayFF (including partial adaptations from the Interface force field) leads to deviations of 20% in surface energies and 100% in bulk modulus relative to experiments (Table 1). Also, DFT methods perform with variable accuracy, or require lengthy testing of suitable density functionals (revised PBE used here) (Table 1). Deviations in density exceed 10%, large deviations in surface energies up to 100% are seen, and the bulk modulus shows 10% to 30% deviation (Table 1). Errors of this magnitude using common density functionals are also known for metals, oxides, and other compounds.[66, 67] Improvements can be achieved with DFT-D, which better accounts for van-der-Waals interactions using added fit parameters for dispersion.[66, 67] The underlying electron-electron interactions are difficult to embed in density functionals otherwise (PBE, revPBE, LDA). While DFT-D tends to be more reliable (e.g., gypsum in Table 1), different approaches have been suggested and the physical interpretation remains somewhat ambiguous.[66-68] In summary, existing models may be best described as curve fits with limited

internal consistency and, as a result, low accuracy and transferability. Major shortcomings are the neglect of underlying chemical detail and a missing interpretation of the Hamiltonian.

The new parameters in the Interface Force Field (IFF) take an entirely different approach and perform at least one order of magnitude better (errors lower by a factor of 10). We include the correct balance of covalent bonding versus ionic bonding, the validation of structure, surface energies, interfacial energies, energy derivatives, as well as full interpretation and thermodynamic consistency of the parameters.[20, 51, 69, 70] A first set of consistent parameters and surface models for gypsum (dihydrate) and bassanite (hemihydrate) was introduced in ref. [20] and evolved into the version presented here. This complete set of force field parameters and validation for hydrous calcium sulfate phases has far higher reliability in comparison to prior models and full compatibility with existing force fields for organic compounds (IFF, AMBER, CHARMM, CVFF, DREIDING, OPLS-AA, PCFF). Typical deviations relative to experiment are <1% in lattice parameters and density, <5% in surface energies, and <5% in mechanical and thermal properties (see summary in Table 1 as well as Tables S2 and S3 in the Supplementary Information).

The force field parameters and surface models allow accurate simulations of calcium sulfate minerals and complex hybrid materials in atomic resolution up to the 1000 nanometer scale for quantitative insights into cleavage, hydration, phase transformations, mechanics, interaction with organic compounds, and thermal expansion. Molecular models and all-atom force field parameters for calcium sulfate minerals are described in section 2. In section 3, computed structural and vibrational properties of the $CaSO_4 \cdot xH_2O$ phases are reported and compared to experiment. In section 4, (h k l) cleavage energies, solid-liquid interfacial energies, and immersion energies are presented and interpreted at the molecular scale, including validation by available experimental

data. Conclusions follow in section 5. Full computational details, models, force field files, and additional information on calcium sulfate crystal structures are provided in the Supplementary Information. Insights into phase equilibria upon hydration and dehydration, mechanical and thermal properties, and organic interfaces are discussed in a follow-on publication.[71]

Table 1. Comparison of key structural and energetic properties of calcium sulfates according to experiment, the new force field (IFF), earlier force fields, and DFT. The reliability is much improved over earlier models.

Minerals	Properties	Experiment	IFF (LJ 9-6)	COMPASS	CVFF	ReaxFF[a]	CHARMM	ClayFF-IFF	DFT[b]
Anhydrite	Lattice parameters (nm) and density ρ (g/cm^3)	a = 2.098,	2.119,	2.060,	2.181,	2.168	2.024,	2.108	2.160
		b = 2.098,	2.052,	1.977,	2.082,	2.169	2.020,	2.098	2.178
		c = 1.873,	1.895,	1.760,	1.786,	1.931	1.923,	1.895	1.927
		$\alpha = \beta$ = 90°	90°, 90°	90°, 90°	90°, 90°	90°,90°	90°, 90°	90°, 90°	90°, 90°
		γ = 90°	90°	90°	90°	90°	90°	90°	89.83°
		ρ = 2.960 [26]	2.963	3.403	3.009	2.682	3.103	2.911	2.69
Bassanite		a = 2.406,	2.407,	2.311,	2.435,	2.406	2.351,	2.401	2.488
		b = 2.078,	2.076,	1.987,	2.086,	2.701	2.028,	2.078	2.173
		c = 2.534,	2.501,	2.376,	2.508,	25.068	2.538,	2.597	2.596
		$\alpha = \gamma$ = 90°	90°, 90°	90°, 90°	90°, 90°	90°, 90°	90°, 90°	90°, 90°	90°, 90°
		β = 90.27°	90.29°	90.68°	91.32°	90.27	90.23°	90.36°	90.2°

Gypsum		ρ = 2.739 [25]	2.778	3.181	2.725	0.554	2.868	2.678	2.473
		a = 1.703, b = 1.521, c = 1.886, $\alpha = \gamma$ = 90° β = 114.08° ρ = 2.307 [27, 50]	1.698, 1.494, 1.876, 90°, 90° 110.0° 2.302	1.607, 1.467, 1.750, 90°, 90° 112.49° 2.700	1.690, 1.521, 1.886, 90°, 90° 115.11° 2.359	1.957 39.46 2.035 86°, 89° 108.2° 0.138	1.645, 1.485, 1.907, 90°, 90° 113.08° 2.401	1.679 1.509 1.911 90°, 90° 114.57° 2.337	1.704[e] 1.518[e] 1.913[e] 90°, 90°[oe] 114.3°[oe] 2.271[e]
Anhydrite (hkl)[c]	Surface energy (mJ/m^2)	NA	542 ± 20 (1 0 0)	765 ± 49 (1 0 0)	665 ± 7 (1 0 0)	0.0 (1 0 0)	473 ± 6 (1 0 0)	895 ± 2 (1 0 0)	273 ± 10 (1 0 0)
Bassanite (hkl)		NA	390 ± 32 (0 0 1)	277 ± 2 (0 0 1)	309 ± 7 (0 0 1)	0.0 (0 0 1)	292 ± 5 (0 0 1)	493 ± 3 (0 0 1)	846 ± 10 (0 0 1)
Gypsum (hkl)		365 ± 25 (facet-	348 ± 20 (facet avg.)	258 ± 6 (0 1 0)	219 ± 7 (0 1 0)	0.0 (0 1 0)	231 ± 3 (0 1 0)	331 ± 4 (0 1 0)	300 ± 10[e] (0 1 0)

		average) [38-40]	271 ± 15 (0 1 0)						
Anhydrite	Bulk modulus (GPa)	55 ± 3 [28, 29, 44]	58 ± 3	60 ± 3	89 ± 5	165	56 ± 5	106 ± 8	50 ± 1
Bassanite		52.4 [30, 44]	53 ± 2	68 ± 2	63 ± 3	0.0	56 ± 2	89 ± 4	36 ± 1
Gypsum[d]		44 ± 1.5 [29, 44]	44 ± 1	48 ± 5	49 ± 1	0.383	28 ± 2	64 ± 4	44 ± 1[e]

[a] From ref. [72], which contains S, O, Ca, and water. Several phases and surfaces are unstable. [b] Revised PBE functional, ultrasoft pseudopotential, 380 eV energy cutoff, 2x2x2 k points, geometry optimization with 200 cycles, $5 \cdot 10^{-7}$ eV/atom convergence, CASTEP program. The bulk modulus was calculated at 0.5 GPa stress using a difference in volume. [c] Values for the lowest energy (hkl) surface are given. See details in Table 4. [d] See details of mechanical properties in Table S2 in the Supplementary Information and in ref. [71]. [e] We report recent values using DFT-D (Tkatchenko and Scheffler) from ref. [68] instead of revPBE. Deviations with revPBE and other DFT-D functionals can be significant, e.g., revPBE yields lattice parameters of a = 1.742 nm, b = 1.567 nm, c = 1.970 nm, $\alpha = \gamma = 90°$, β = 113.3°, a density of 2.084 g/cm^3, a (010) surface energy of 143 ± 10 mJ/m^2, and a bulk modulus of 31 ± 1 GPa.

2. Force Field Parameterization

2.1. Potential energy expressions

We derived force field parameters that can be used with the common polynomial energy expressions CFF, PCFF,[73, 74] COMPASS (eq 1),[75] CHARMM,[76] AMBER,[22, 77] CVFF,[78] DREIDING, and OPLS-AA[79] (eq 2). The potential energy of the system E_{pot} is the sum of energy contributions for quadratic bond stretching (E_{bonds}), quadratic angle bending (E_{angles}), as well as electrostatic ($E_{Coulomb}$) and van-der-Waals interactions (E_{vdW}) between atoms. E_{pot} depends only on the Cartesian coordinates of the atoms along the directions of the three coordinate axes. The parameters q_i, $r_{0,ij}$, $\theta_{0,ijk}$, $K_{r,ij}$, $K_{\theta,ijk}$, ε_{ij}, and σ_{ij} used in eq 1 and eq 2 make up the force field and represent atomic charges, equilibrium bond lengths, equilibrium bond angles, vibrational constants for bond stretching, vibrational constants for angle bending, pairwise equilibrium nonbond energy as well as the equilibrium nonbond distance between pairs of atoms, respectively (Table 2).

$$E_{pot} = \sum_{ij\ bonded} K_{r,ij}(r_{ij} - r_{0,ij})^2 + \sum_{ijk\ bonded} K_{\theta,ijk}(\theta_{ijk} - \theta_{0,ijk})^2 + \frac{1}{4\pi\varepsilon_0} \sum_{\substack{ij\ nonbonded \\ (1,2\ \textit{and}\ 1,3\ excl)}} \frac{q_i q_j}{r_{ij}} + \sum_{\substack{ij\ nonbonded \\ (1,2\ \textit{and}\ 1,3\ excl)}} \varepsilon_{ij}\left[2\left(\frac{\sigma_{ij}}{r_{ij}}\right)^9 - 3\left(\frac{\sigma_{ij}}{r_{ij}}\right)^6\right] \quad (1)$$

$$E_{pot} = \sum_{ij\ bonded} K_{r,ij}(r_{ij} - r_{0,ij})^2 + \sum_{ijk\ bonded} K_{\theta,ijk}(\theta_{ijk} - \theta_{0,ijk})^2 + \frac{1}{4\pi\varepsilon_0} \sum_{\substack{ij\ nonbonded \\ (1,2\ \textit{and}\ 1,3\ excl)}} \frac{q_i q_j}{r_{ij}} + \sum_{\substack{ij\ nonbonded \\ (1,2\ \textit{and}\ 1,3\ excl)}} \varepsilon_{ij}\left[\left(\frac{\sigma_{ij}}{r_{ij}}\right)^{12} - 2\left(\frac{\sigma_{ij}}{r_{ij}}\right)^6\right] \quad (2)$$

The polynomial energy expressions shown in eq 1 and eq 2 are applicable to metals, ceramics, and soft matter, including additional torsion and out-of-plane terms for biomacromolecules.[20] The parameters can be assigned a clear physical-chemical interpretation. Parameters for 9−6 Lennard-Jones potentials (eq 1) and 12−6 Lennard-Jones potentials (eq 2) differ slightly for algebraic reasons, as well as due to specific combination rules to obtain σ_{ij} and ε_{ij} for pairs of different atom types i and j from the homoatomic interaction parameters σ_{ii} and ε_{ii} listed in Table 2. The combination rules follow the conventions for the respective force field.[20] Specific scaling rules for nonbonded interactions between 1, 4 bonded atoms in various force fields play no role for calcium sulfates as there are no 1, 4 bonded atoms present. Differences in combination rules among force fields using a 12-6 LJ potential (CHARMM, AMBER, OPLS-AA, CVFF) are also small. Therefore, for calcium sulfates, one parameter set for all force fields using a 12-6 LJ potential and one parameter set for FFs using a 9-6 LJ potential are sufficient.

Table 2. Force field parameters for calcium sulfate phases using an energy expression with a 9-6 Lennard-Jones potential (equation 1, PCFF, COMPASS) and with a 12-6 Lennard-Jones potential (equation 2, CHARMM, CVFF, AMBER, OPLSA-AA, DREIDING, GROMOS).

		9-6 LJ Parameters (eq 1)		12-6 LJ Parameters (eq 2)	
I. Nonbond	Charge (e)	$\sigma_{0,ii}$ (pm)	$\varepsilon_{0,ii}$ (kcal/mol)	$\sigma_{0,ii}$ (pm)	$\varepsilon_{0,ii}$ (kcal/mol)
Ca	+1.7	355	0.24	310	0.22
S	+0.5	445	0.30	420	0.30
$O^{sulfate}$	–0.55	350	0.06	340	0.12
O^{water}	–0.82	360.8 [a]	0.274 [a]	355.3[b]	0.155[b]
H^{water}	+0.41	109.8 [a]	0.013 [a]	0.0 [b]	0.0 [b]
II. Bonds		r_0 (pm)		K_r [kcal/(mol·Å^2)]	
S–O		150.5		380	
O–H: 9-6 LJ[a]		97		520.00 (k_2), –1282.90 (k_3), 1902.12 (k_4)[a,c]	
O–H: 12-6 LJ[b]		96		540.63	
III. Angle		θ_0 (°)		K_θ [kcal/(mol·rad^2)]	
O–S–O		109.5		170	
H–O–H: 9-6 LJ[a]		103.7		49.84 (k_2), –11.60 (k_3), –8.00 (k_4)	
H–O–H: 12-6 LJ[b]		104.5		50.0	

[a] Parameters for the standard PCFF water model are listed and used here.

[b] Parameters for a flexible SPC water model are listed and used. Other standard SPC or TIP3P parameters for water can also be used without significant changes in performance (even when including slightly different atomic charges).

[c] Original PCFF parameters for bond stretching were modified to precisely reproduce the IR vibrations of water near 3489 cm^{-1}. The original parameters can also be used [563.28 (k_2), –1428.22 (k_3), 1902.12 (k_4)], then not reproducing this particular IR band.

2.2. Derivation of the atomistic force field

The development of force field parameters for calcium sulfates followed the IFF approach that involves well defined steps for the derivation and interpretation of each parameter.[7, 16, 20, 69, 80, 81] We present a single set of parameters for all calcium sulfate phases, and no further customized force field types for each compound. This approach leads to a minor compromise in accuracy which is, however, well within the limits of the accuracy of water models. The broadly applicable calcium sulfate models (also extensible for Mg and other sulfates) enable the study of reversible hydration and dehydration reactions among all calcium sulfate phases, as well as interactions with chemical additives, polymers, and biomacromolecules.

The first step was the selection of reliable crystal structures from X-ray or Neutron diffraction data (Figure 2).[2] We chose X-ray diffraction data by Hawthorne et al.[26] for thermodynamically stable β-anhydrite (Figure 2a), X-ray data by Bezou et al.[25] for bassanite (Figure 2b), and neutron diffraction data for the monoclinic crystal structure of gypsum by Pedersen and Semmingsen[27] with the space group *A2/a* (Figure 2c). Differences to other proposed space groups for gypsum are minor and captured by the force field (see Table S1 and Section S1 in the

Supplementary Information).

We employ five atom types for Ca^{2+} ions, S and O atoms in sulfate ions, H and O atoms in H_2O (Figure 2d). Assignment of atomic charges for calcium ions, sulfate ions, and water represents the magnitude of ionic versus covalent bonding,[65] and was carefully undertaken as the surface energy depends on the square of the atomic charges and on the cation density of cleaved planes. The calcium charge is +1.7e out of +2e as a maximum formal charge as there are some covalent contributions to bonding, similar to calcium oxide, calcium silicates, and calcium phosphates consistent with experimentally measured electron deformation densities and theory.[7, 16, 20, 51, 80, 82] We also tested a +1.6e charge of Ca^{2+} instead of +1.7e, which leads to approximately 10-15% underestimates in cleavage energies, elastic moduli, and overestimated thermal expansion of the calcium sulfate phases, and such deviations are near 0% with +1.7e. Calcium sulfate minerals have thus slightly more ionic character than previously studied calcium-containing minerals such as tricalcium silicate, tricalcium aluminate and hydroxyapatite with Ca charges of +1.5e to +1.6e.[7, 16, 80, 83] For the crystal structures of calcium sulfate phases considered in this paper, Ca^{2+} ions and the square-antiprismatic coordination shell of 8 oxygen atoms by water and sulfate are described by nonbonded-only terms. The reason is that Ca···O distances are in a range from 2.366 Å to 2.552 Å that is typical for noncovalent bonds, and the Ca^{2+} atomic charge is clearly more than 50% on the ionic side of the spectrum of pure covalent bonding to pure ionic bonding.

The atomic charge for S in tetrahedral oxygen coordination is +0.5 ± 0.1e. This value is consistent with known similar charges of +1.2e for Al,[7] +1.1e for Si,[81] +0.8e for C,[51] and +1.0e for P in tetrahedral oxygen coordination, higher electronegativity of S, and a net negative charge on SO_4^{2-} ions that somewhat reduces the positive charge on the S atom.[16, 20] The degree

of ionic bonding also correlates with trends in atomization energies and electronegativity for the neighbor elements in the periodic table as represented by the extended Born model.[51, 84] The negative charges in ions such as silicate, phosphate, and sulfate warrant even lower positive charges at the center atoms (Si, P, S) of +1.0e,[80] +0.8e, and +0.5e.[51] Ultimately, these charge distributions represent chemical bonding and verifiable internal multipole moments. The atomic charge of the oxygen atoms in sulfate ions then results as –0.55e due to charge neutrality, leading to an overall charge of –1.7e for sulfate ions in the solid state. S–O bonds in sulfate ions are clearly covalent in nature as atomic charges in S and O are both less than half of their formal charges, and S–O bond lengths of 1.48 Å are in the expected range for covalent bonds.[85] S–O bonds are therefore represented by bonded and nonbonded parameters. Exact bond distances between S and O are slightly different in anhydrite (1.473 ± 0.001 Å), bassanite (1.48 ± 0.01 Å) and gypsum (1.472 ± 0.001 Å),[25-27] yet close enough to be described with a single set of parameters. Structural features such as square-antiprismatic $Ca(\cdots O)_8$ arrangements and sulfate tetrahedra in gypsum crystals are similarly found in anhydrite (*Amma* space group),[26, 27, 82] and in the coordination environment in monoclinic bassanite.[30] Similarity in composition and atomic arrangements support the use of one set of force field parameters including atomic charges for calcium sulfate phases regardless of their water content.

Lennard-Jones parameters were assigned according to known trends in atomic/ionic radii (σ_{ii}), atomic polarizabilities and coordination environment (ε_{ii}).[20, 85, 86] In the final optimization of cell parameters, only minor changes in the LJ parameters were required to reproduce the lattice parameters (a, b, c, α, β, γ) and atomic distances during NPT molecular dynamics simulation in agreement with X-ray and neutron diffraction data (Table 3). Nevertheless, we carried out

extensive tests of nonbond diameters σ_{ii} and well depths ε_{ii} to achieve a consistent match for all three minerals. For example, LJ 9-6 potentials suitable for gypsum yield a slightly higher density for bassanite, and a better match could be achieved by minor variations of LJ parameters for the two minerals. However, we believed that the benefit of consistent parameters for all mineral phases outweighs the benefits of fixing such small discrepancies.

Bonded terms include S–O bonds and S–O–S angles in the SO_4^{2-} ions as well O–H bonds and H–O–H angles in water molecules (Table 2). Water molecules are described using standard water models following the concept of thermodynamic consistency in IFF, such as SPC (or TIP3P) water models as used in CHARMM, AMBER, and PCFF. The standard water models cause no noteworthy difficulties in force field performance.[20] For the SO_4^{2-} ions, equilibrium bond lengths $r_{0,ij}$ and equilibrium bond angles $\theta_{0,ijk}$ (eq 1 and eq 2) were selected from neutron diffraction and X-ray data.[25-27] Minor adjustments of $r_{0,ij}$ and $\theta_{0,ijk}$ relative to bond lengths and angles from scattering data were made (<3%) to account for the superposition with nonbonded energy terms in the force field (Table 2). X-ray data also suggest small deviations of the geometry of sulfate ions from a regular tetrahedron in all three minerals.[25-27] The force field reproduces average bond lengths and bond angles in NPT molecular dynamics simulations with <2% deviation from experiment, as well as the lattice parameters of the minerals (Table 3).

Vibration constants $K_{r,ij}$ and $K_{\theta,ijk}$ were initially estimated according to known force constants of similar molecules and refined to be consistent with measured IR spectra of anhydrite and gypsum[45, 87, 88] using the Fourier transform of the velocity autocorrelation function (Figure 3).[7, 80, 81] We also tested specific improvements in bond stretching constants $K_{r,ij}$ and its 3rd and 4th power additions in the PCFF water force field (Table 2, footnote c) to best reproduce the

experimental O–H stretching vibration of H_2O in gypsum crystals near 3489 cm^{-1}. However, such adjustments are not necessary for most purposes.

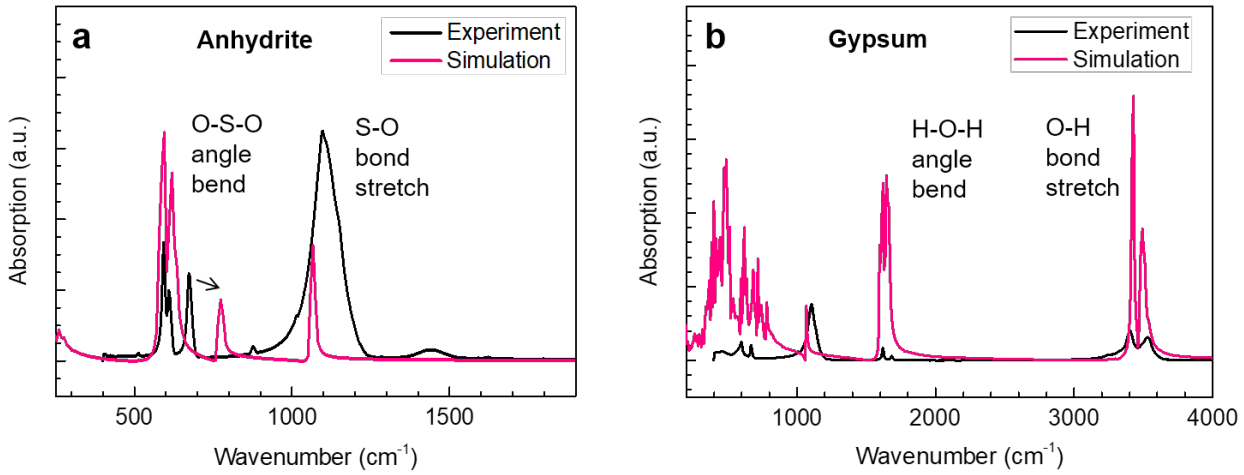

Figure 3. Vibration spectra computed from molecular dynamics simulation (superposition of IR and Raman) in comparison with experimental IR data.[45, 87, 88] (a) Anhydrite. (b) Gypsum. The arrow in (a) indicates a deviation in the classical model. Results are similar for bassanite (not shown).

2.3. Refinement and Validation

Key targets for the refinement of force field parameters are the lattice parameters for all minerals, the cleavage energies, as well as reported bulk moduli in comparison to experiment. Once these were reproduced quantitatively, remaining properties such as solid-water interfacial energies and thermal properties were obtained in agreement with experiment without further assumptions or refinements. The agreement demonstrates impressive consistency of the force field in comparison

to other models (Table 1), whereby atomic charges,[51] bonded parameters,[81] and $\sigma_{0,ii}$ [86] are associated with a physical-chemical rationale and adjustable only in a small percentage range.[17] The well depths $\varepsilon_{0,ii}$ as well as the $\sigma_{0,ii}/\varepsilon_{0,ii}$ ratio have somewhat more flexibility (see ref. [20]) and, for example, affect the hydration energy of Ca^{2+} ions.

Parameter refinement and testing involved over 1000 individual calculations in total. The stability of the force field was thoroughly tested for large structures (>10 nm) and long simulation times (>100 ns). The average accuracy is ~1% in lattice parameters and the reliability of cleavage energies, hydration energies, and bulk moduli is essentially the same as the experimental uncertainty of ±5%. The performance thereby exceeds the capabilities of common DFT methods for the same systems. In addition, IFF is applicable to systems more than a million times larger in length and time scale.

3. Structural and Vibrational Properties

NPT molecular dynamics simulations under ambient conditions yield an average S–O bond length of 1.48 ± 0.02 Å for the three minerals, which agrees with average bond lengths of 1.473 ± 0.001 Å, 1.48 ± 0.01 Å, and 1.472 ± 0.001 Å for anhydrite, bassanite, and gypsum, respectively, from X-ray data.[25-27] Computed lattice parameters and densities in NPT molecular dynamics deviate on average <1% from experiment, and often less than 0.5% (Table 3). Differences in crystal symmetry of the minerals are also very well preserved in the simulation. The performance of force fields with 9-6 or 12-6 Lennard-Jones potentials (eq 1 and eq 2) is about the same.

Limitations include, for example, a slight extension of the anhydrite simulation cell along the *a*-axis (+1% to +2%) and a contraction of the *b*-axis (–2%). Similar small offsets are seen for bassanite (calcium sulfate hemihydrate) while cell angles are precisely reproduced. Gypsum lattice parameters in the simulation follow closely experimental data except for the cell angle *β*. Some of the percent-range deviations in the hydrated sulfates (bassanite, gypsum) are related to known limitations of the water models.[89]

Table 3. Lattice parameters of anhydrite,[26] bassanite[25] and gypsum[27, 50] crystals according to experiment and NPT molecular dynamics simulation using IFF parameters in 9-6 LJ form (compatible with PCFF, COMPASS) and in 12-6 LJ form (compatible with AMBER, CHARMM, CVFF, OPLS-AA) under standard temperature and pressure.

Mineral	Method	Cell dim.	*a* (nm)	*b* (nm)	*c* (nm)	*α* (°)	*β* (°)	*γ* (°)	*V* (nm^3)	*ρ* (g/cm^3)
Anhydrite	Exptl[26]		2.0979	2.0985	1.8735	90	90	90	8.2479	2.9601
	Sim 9-6[a]	3×3×3	2.119	2.052	1.895	90	90	90	8.241	2.963
	Sim 12-6		2.142	2.058	1.873	90	90	90	8.258	2.957
Bassanite	Exptl[25]		2.4063	2.0781	2.5342	90	90.27	90	12.672	2.7387
	Sim 9-6	2×3×2	2.407	2.076	2.501	90	90.29	90	12.495	2.778
	Sim 12-6		2.437	2.098	2.483	90	90.45	90	12.670	2.733
Gypsum	Exptl[27, 50]	3×1×3	1.7034	1.5213	1.8858	90	114.08	90	4.4616	2.3068

Sim 9-6	1.698	1.494	1.876	90	110.0	90	4.471	2.302
Sim 12-6	1.703	1.521	1.856	90	112.1	90	4.455	2.310

[a] "Sim 9-6" refers to energy expressions using the 9-6 LJ potential (eq 1). "Sim 12-6" denotes energy expressions using the 12-6 LJ potential (eq 2).

The calculation of vibration spectra from MD simulation shows good agreement in wavenumbers, though not in intensities, with measured IR spectra for the calcium sulfate hydrates (Figure 3).[45, 87, 88] Vibrations at 600−700 cm^{-1} correspond to O−S−O angle bending, weaker bands at 1000 cm^{-1} to the symmetric S−O bond stretching vibrations, and the strong band at 1050−1250 cm^{-1} to asymmetric S−O bond stretching vibrations. The agreement is typically better than 50 cm^{-1} in wavenumbers although the computed value for one of the bands in anhydrite near 700 cm^{-1} is shifted approximately 100 cm^{-1} higher, or might represent a Raman peak near 700 cm^{-1} (Figure 3a).[87, 88] In gypsum, the strong band for asymmetric S−O bond stretching is found at slightly lower wavenumbers of 1050−1150 cm^{-1} due to hydrogen bonds with water (Figure 3b). Vibrational bands at 1600−1700 cm^{-1} as well as at 3395 and 3489 cm^{-1} appear due to the presence of water and correspond to H−O−H angle bending and O−H bond stretching vibrations, respectively. The peaks can be reproduced using tailored vibration constants $K_{r,ij}$ and $K_{\theta,ijk}$ in the energy expression (Table 2).

It is a generally accepted limitation that fine details such as exact wavenumbers and intensities are not captured in all-atom force fields because details of the electronic structure are not included for simplicity and high computational speed.[45, 87, 88] For the calcium sulfates minerals

described here, we use only four harmonic parameters (Table 2) to reproduce the entire vibration spectrum (Figure 3). The performance is quite good for this level of simplification, and relative differences in wavenumbers due to changes in chemical environment can still be meaningfully compared between computation and experiment.

4. Surface and Interfacial Energies

4.1. Surface Energy

Accurate surface and interfacial energies are the key to predicting solubility, adsorption, and surface reactions in computational models.[17] The cleavage energy equals the surface energy of a solid when no surface reconstruction occurs during the measurement time.[81] The cleavage energy is also a reproducible measure of cohesion of a solid under standard conditions even if surface reconstruction occurs.[17] Possible (h k l) cleavage planes of the calcium sulfates are shown in Figures 4, 5, and 6, and hitherto unknown values of facet-specific cleavage energies are reported here (Table 4). The cleaved surfaces of calcium sulfates show only minor rearrangements of ions and water in molecular dynamics simulations (Figure S1 in the Supplementary Information). The crystal-average surface energy of gypsum obtained by simulations is 348 ± 15 mJ/m^2. The value is in excellent agreement with experimental measurements of 365 ± 25 mJ/m^2 (Table 4) [38-40] and confirms the ability of the force field to predict energy differences correctly.

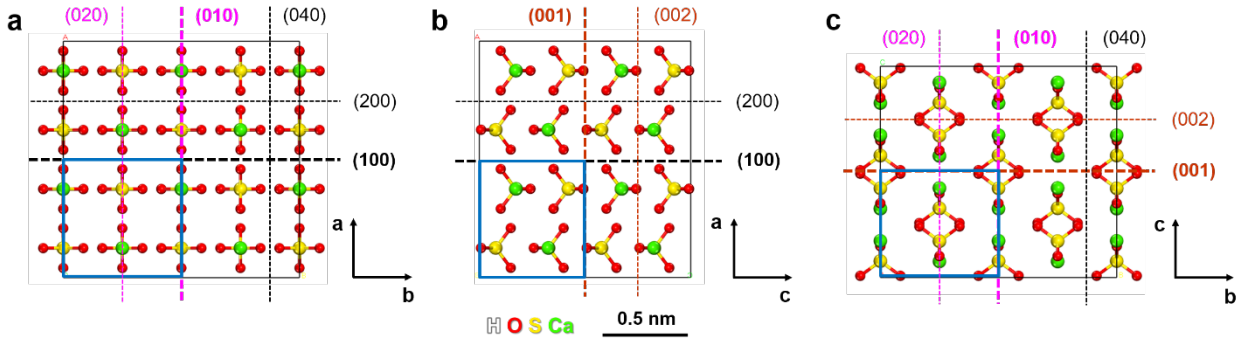

Figure 4. Possible cleavage planes in anhydrite ($CaSO_4$) shown in a (2×2×2) super cell. Unit cell dimensions are displayed by blue solid lines. Black dashed lines indicate the (1 0 0) plane and the equivalent (2 0 0) and (0 4 0) cleavage planes of lowest energy. Brown dashed lines visualize the (0 0 1) plane and the equivalent (0 0 2) cleavage plane of intermediate energy. Pink dashed lines highlight the (0 1 0) plane and the equivalent (0 2 0) cleavage plane of higher energy. (a) Cleavage planes perpendicular to the *ab* plane; projection perpendicular to the *c* axis. (b) Cleavage planes perpendicular to the *ac* plane; projection perpendicular to the *b* axis. (c) Cleavage planes perpendicular to the *bc* plane; projection perpendicular to the *a* axis.

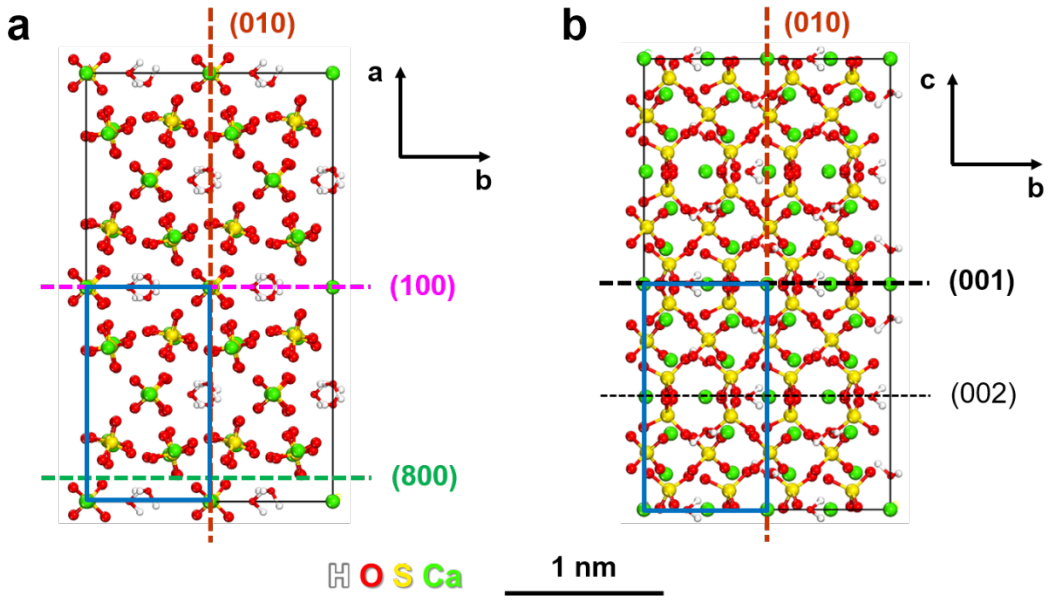

Figure 5. Possible cleavage planes in bassanite ($CaSO_4 \cdot ½ H_2O$) drawn in a (2×2×2) super cell. Unit cell dimensions are indicated by rectangular boxes with blue solid lines. The black dashed lines indicate the (0 0 1) and (0 0 2) planes of lowest energy, brown dashed lines highlight the (0 1 0) plane of intermediate energy. Pink and green dashed lines denote (1 0 0) and (8 0 0) cleavage planes of high energy. (a) Cleavage planes perpendicular to the *ab* plane; projection perpendicular to the *c* axis. (b) Cleavage planes perpendicular to the *bc* plane; projection perpendicular to the *a* axis.

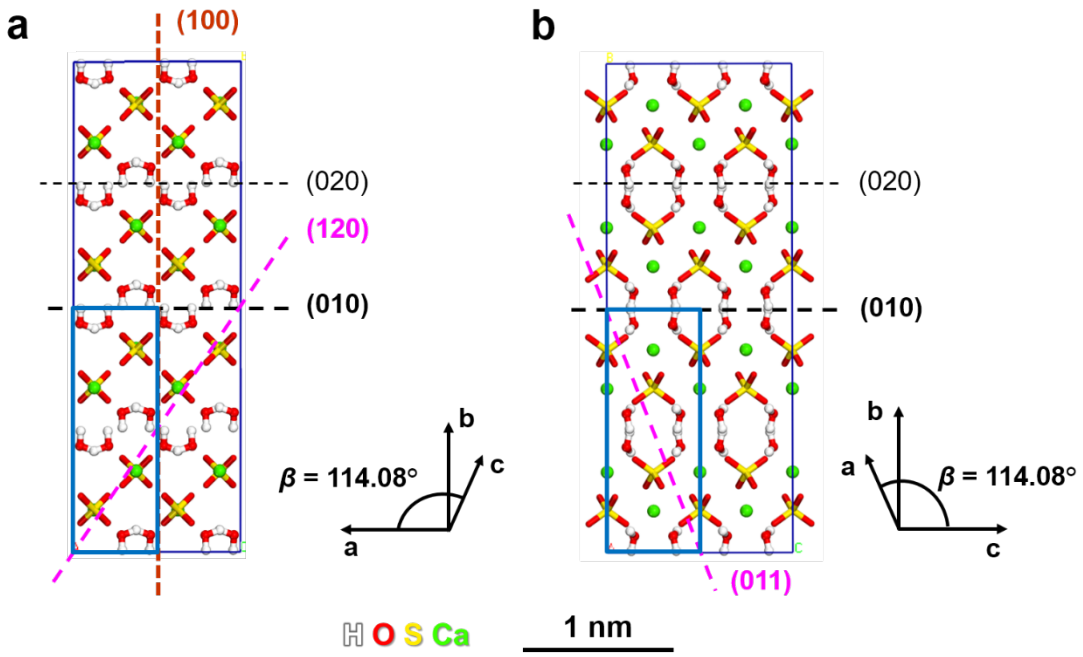

Figure 6. Observed cleavage planes in gypsum ($CaSO_4 \cdot 2\ H_2O$) shown in a (2×2×2) super cell. Unit cell dimensions are illustrated by rectangular boxes with blue solid lines. Black dashed lines denote the (0 1 0) plane and the equivalent (0 2 0) plane of lowest energy. The brown dashed line indicates the (1 0 0) plane of intermediate energy. The (–1 1 1) plane of somewhat higher energy is not shown (requires 3D view). The pink dashed line shows the (1 2 0) and (0 1 1) cleavage planes of higher energy. (a) Cleavage planes parallel to the *c* axis; crystal structure projected perpendicular to the *c* axis (approximately in the *ab* plane). (b) Cleavage planes perpendicular parallel to the *a* axis; crystal structure projected perpendicular to the *a* axis (approximately in the *bc* plane).

Table 4. Computed cleavage energy (surface energy) of various Miller planes of anhydrite, bassanite and gypsum, listed in the order of ascending values. Equivalent crystallographic planes with the same cleavage energy are indicated.

Mineral and (h k l) plane	Cleavage energy	
	Computed (mJ/m^2)	Experimental (mJ/m^2)
Anhydrite (1 0 0), (2 0 0), (0 4 0)	542 ± 20[a], 535 ± 20[b]	
Anhydrite (0 0 1), (0 0 2)	600 ± 23	
Anhydrite (0 1 0), (0 2 0)	686 ± 30	
Bassanite (0 0 1), (0 0 2)	390 ± 32[a], 370 ± 20[b]	
Bassanite (0 1 0)	578 ± 25	
Bassanite (1 0 0)	784 ± 30	
Bassanite (8 0 0)	870 ± 40	
Gypsum (0 1 0), (0 2 0)	271 ± 15[a], 263 ± 20[b]	
Gypsum (1 0 0)	417 ± 26	
Gypsum (–1 1 1)	530 ± 20	
Gypsum (1 2 0)	567 ± 20	
Gypsum (0 1 1)	600 ± 23	
Gypsum crystal, facet-average	348 ± 20,[c] 341 ± 16[c]	365 ± 25[d]

[a] Using the energy expression with a LJ 9-6 potential. [b] Using the energy expression with a 12-6 LJ potential. Results with 12-6 and 9-6 LJ potentials are identical within error bars. [c] Equilibrium facet-average is assumed according to equations (9) and (10) (see also Figure 7b). [d] Refs. [38-40].

The simulations also indicate that equilibrium cleavage involves equal partition of calcium and sulfate ions between the newly created surfaces, consistent with observations for other minerals.[16, 80, 90, 91] Low energy surfaces display minimal local electric fields and result from (h k l) cleavage planes that require minimal, or no separation of intimate ion pairs and multipolar local charge distributions. Cleavage energies consist over 80% of Coulomb energy and the maximum contribution of van-der-Waals energy is around 50 mJ/m^2. Significant interactions subside after 1 to 2 nm surface separation. In case of nonequilibrium, unequal partition of ions, cleavage energies can exceed several 1000 mJ/m^2 and extend the range of notable attraction beyond 10 nm.

Specifically, in anhydrite, the (1 0 0), (2 0 0), and (0 4 0) cleavage planes are equivalent and exhibit the lowest cleavage energy of ~540 mJ/m^2 according to the simulation (Figure 4). No separation of ions is required during cleavage of this plane. The (1 0 0) plane has been observed in atomic force microscopy (AFM)[27, 48, 49] and, consistently, the AFM data indicate near-perfect cleavage as well as much higher stability in comparison to (0 0 1) and (0 1 0) planes (Figure 4a,b).[27, 48] The next highest cleavage energy of ~600 mJ/m^2 was computed for the (0 0 1) plane (Figure 4b,c). The (0 0 1) plane does also not require separation of ions across the cleaved surface, nevertheless, it was harder to generate in AFM measurements.[48] Finally, cleavage of the (0 1 0) plane requires equal partitioning of calcium and sulfate ions, and the higher ionic density increases the surface energy to ~690 mJ/m^2 (Figure 4a,c). AFM measurements mention a high, or highest, stability of surfaces in the "(0 1 0)" direction, however, these are likely the (0 4 0) surfaces that are identical to the (1 0 0) surfaces of lowest energy due to crystal symmetry (see Figure 4).[48, 49] Therefore, the overall ranking of facet stability according to AFM data is (0 4 0) ≈ (1 0 0) > (0

0 1) and molecular dynamics simulations have quantified the surface energies as (0 4 0) = (1 0 0) < (0 0 1) < (0 1 0) consistent with these observations.

In bassanite (calcium sulfate hemihydrate), cleavage energies are lower relative to anhydrite due to the presence of water molecules (Figure 5, Table 4). The plane of lowest energy is the (0 0 1) plane with ~380 mJ/m^2. Cleavage involves only the distribution of Ca^{2+} ions and water molecules and is therefore comparatively low-energetic (Figure 5b). The next highest energy was found for the (0 1 0) plane. Due to the distribution of both sulfate and calcium ions, the energy is markedly higher at 580 mJ/m^2 (Figure 5a,b). Distribution of Ca^{2+} and sulfate ions is also required for the (1 0 0) plane that carries a slightly higher ion density per unit area. Accordingly, the cleavage energy increases to 780 mJ/m^2 (Figure 5a). Finally, the (8 0 0) plane was found to be energetically unfavourable due to a charge imbalance upon separation of the slabs. The charge imbalance could be neutralized with the help of temperature gradient MD simulations that allows transfer of ions and surface reconstruction, resulting in an energy of 840 mJ/m^2 (Table 4). While specific experimental data for calcium sulfate hemihydrate are rare, the increased anisotropy of surface energies helps explain the observed rod-like crystal habit of α-hemihydrate.[1, 47] The rod-like crystal shape in *x* or *y* direction includes low-energy (001) bounding facets, and also engages further surrounding facets such as (0 1 1)/(0 –1 1) and (1 0 1)/(–1 0 1), respectively, which may be explored in follow-on studies.

Gypsum displays a well-known (010) cleavage plane of minimum energy (Figure 6a,b).[55, 92, 93] Equal partitioning of a double layer of water molecules eases cleavage and MD simulations identified a low cleavage energy of 270 ± 15 mJ/m^2 (Table 4). The (0 1 0) or (0 2 0) planes, therefore, constitute the majority of the surface area of macroscopic gypsum crystals (Figure

7).[92, 94-96] The (1 0 0) plane is of about 50% higher surface energy of ~420 mJ/m^2. Other known cleavage planes of gypsum include (–1 1 1), (1 1 1), (1 2 0), (0 1 1), (0 –1 1), and the associated surface energies are even higher in the range of 500 to 600 mJ/m^2 (Figure 6a,b and Table 4). For example, the (–1 1 1) plane involves separation of Ca^{2+} and water and is associated with a cleavage energy of 530 mJ/m^2 (not shown). Similarly, the (1 1 1) plane includes sulfate ions near to the cleavage plane. Cleavage of the (1 2 0) plane separates sulfate ions as well as calcium ions and requires 570 mJ/m^2 (Figure 6a). The (0 1 1), (0 –1 1), and (0 1 –1) cleavage planes are identical and exhibit a cleavage energy of 600 mJ/m^2 (Figure 6b). Higher surface energy is associated with equal partition of water, sulfate ions, and calcium ions closer to the cleavage plane. Gypsum crystals were also found to display (1 2 –1) and (1 1 0) facets.[96] The common observation of (h k l) facets that possess high cleavage energies and are therefore among the least stable in air or vacuum is owed to their stability in water where gypsum crystals are usually grown (see following sections). Details of the computation of cleavage energies are described in section S2.4 in the Supplementary Information.

The relationship between cleavage energies $\frac{\Delta E_{Cleav}}{A}$ used to describe solid-vapor interfacial energies and surface free energies $\frac{\Delta G_{Cleav}}{A}$ is given by an entropy contribution $\frac{-T\Delta S_{Cleav}}{A}$:

$$\frac{\Delta G_{Cleav}}{A} = \frac{\Delta E_{Cleav}}{A} - \frac{T\Delta S_{Cleav}}{A} \quad (3)$$

A small gain in entropy is expected upon cleavage as ions and molecules near the created surfaces

gain mobility upon cleavage, yet the contribution $\frac{-T\Delta S_{Cleav}}{A}$ is near zero for ions and contributes less than −5 mJ/m^2 in the presence of crystal water, similar to other strongly cohesive, enthalpy-dominated solids.[90, 97] The surface free energy $\frac{\Delta G_{Cleav}}{A}$ is thus up to ~5 mJ/m^2 lower than the surface energy $\frac{\Delta E_{Cleav}}{A}$, which is within the uncertainty of computation (Table 4).

The cleavage energies for all (hkl) surfaces are identical within the error bars using 12-6 and 9-6 LJ potentials (see examples in Table 4). Near-equality is related to internal consistency of the parameters, including structure, energy, and mechanical properties for both parameters sets, and was our goal during the development of all-atom force field parameters.[18, 20] Minor differences originate from the distinct mathematical form.

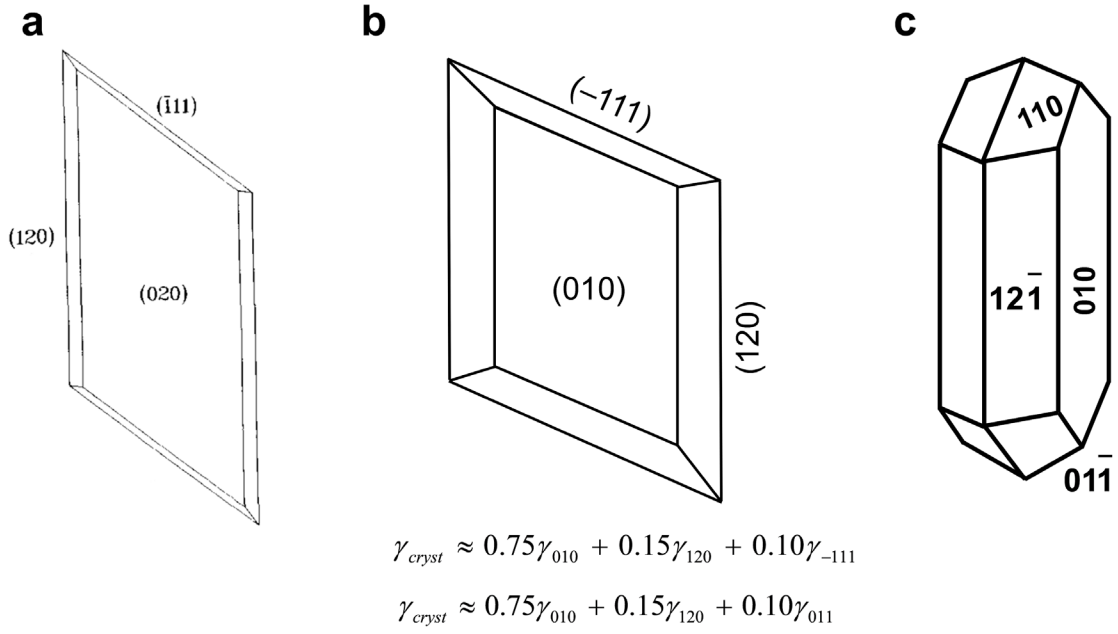

Figure 7. Bounding facets of gypsum crystals. (a) Gypsum habit in aqueous solution (refs. [92, 94, 98]). (b) Equilibrium crystal shape based on experimental observations and optimization of surface energy (Wulff diagram) (refs. [50, 99]). Estimates of the facet-average solid-vapor and solid-liquid interfacial tensions are shown. (c) Alternative crystal shape of gypsum crystals according to known variations in bounding facets and area fractions (refs. [95, 96]).

4.2. Interfacial Energy, Solubility, and Heat of Immersion

Solid-water interfacial energies[41-43] and heats of hydration[100] are key properties of calcium sulfates during crystallization, hydration, and dispersion in wallboard, casts, and medical applications (Figure 1). Interfacial energies $\Delta E_{SL} / A$ and solid-water interfacial tensions $\gamma_{SL} = \frac{\Delta E_{SL} - T\Delta S_{SL}}{A}$ from molecular dynamics simulations are consistent with experimental data

and add strong validation to the force field, including new facet-specific data and mechanistic insight.

Computed interfacial energies $\Delta E_{SL} / A$ and interfacial tensions γ_{SL}, which are approximately +15 mJ/m^2 larger than $\Delta E_{SL} / A$, correlate with the reactivity and solubility of the calcium sulfate minerals in water. Negative values indicate a spontaneous reaction with water (dissolution) while positive values indicate phase boundaries and increasingly lower solubility.[41] Negative interfacial energies were computed for bassanite, small positive interfacial energies for anhydrite, and larger positive interfacial energies for gypsum (Table 5). This trend matches experimental data for reactivity and solubility:[1]

Solubility: Bassanite (6.7 g/l) >> Anhydrite (2.7 g/l) > Gypsum (2.1 g/l) (4)

The correlation of interfacial energies with solubility is consistent with the groundbreaking work by Nielsen et al,[41] and also the experimentally determined, facet-averaged interfacial tension γ_{SL} is known for gypsum to be 76 ± 20 mJ/m^2 from precipitation measurements,[41-43] which agrees perfectly with the computed value from molecular dynamics simulation, 80 ± 10 mJ/m^2 (Table 5). The precipitation measurements rely on nucleation theory and have been consistently applied to sparingly soluble ionic crystals in contact with aqueous solution, considering the hydration of dissolved ions as well as the wetting of the surface of newly forming ionic crystals:[41]

$$\gamma_{SL} = \frac{0.338}{(V_m)^{2/3}}\left[\left(11.6 + \log\frac{t}{s}\right)\log S\right]^{1/2} \qquad \text{(for gypsum)} \qquad (5)$$

whereby V_m is the molar ionic volume in mol/cm^3, t the induction period for mononuclear growth in seconds, and S the initial supersaturation ratio (γ_{SL} was originally designated as σ).

More specifically, for anhydrite, a low positive value of the solid-liquid interfacial energy of 5 ± 9 mJ/m^2 for the (0 1 0) surface is consistent with a slow reaction with water as observed in experiment (eq 4).[100] Interestingly, the same surface has the highest cleavage energy in vacuum among the tested planes and is therefore unlikely formed by cleavage. Typical cleavage planes in air, (1 0 0) and (0 0 1), have less affinity to water with values of $\Delta E_{SL} / A$ of 62 and 100 mJ/m^2, respectively.

Bassanite is the only phase that exhibits a negative solid-liquid interfacial energy of –70 mJ/m^2 (Table 5). This value is observed for the (0 0 1) plane and agrees with rapid spontaneous hydration observed in experiment.[1] The (0 1 0) and (1 0 0) surfaces have a positive interfacial energy of 12 and 97 mJ/m^2 and thus lower affinity to water.

The facets of gypsum display comparatively high solid-liquid interfacial energies in excess of +60 mJ/m^2 for various (h k l) orientations (Table 5), and accordingly gypsum is known to react less readily with water in experiment (equation 4).

The relationships illustrate that the atomically resolved interfacial structure and associated interfacial energy from molecular simulation can be directly related to solubility. For the most reactive bassanite (hemihydrate) phase, central for various applications, the solid-liquid interfacial energies of the different (h k l) surfaces also correlate with the presence of voids and water

channels (Figure 8).[101] Water molecules effectively penetrate (0 1 0) and (0 0 1) surfaces that contain void spaces and pre-existing water channels. In particular, on the (0 0 1) surface with a negative interfacial energy, water molecules in the internal water channels diffuse out of the mineral surface and water molecules from solution enter the interior of the solid phase within nanosecond times scales, accompanied by disorder at the interface (Figure 9). Dissolution of sulfate ions into the aqueous phase typically takes longer than 10 ns. The expected solubility of basanite is 6.7 g/l (46 mM), which equals the dissolution of one sulfate ion and one calcium ion per 1200 water molecules. The dissociation of a few ions in systems the size shown in Figure 9 after longer simulation times is consistent with the expected macroscopic solubility.

Similar to cleavage energies and surface free energies in vacuum, the interpretation of (h k l) specific crystallization and dissolution processes requires a clear distinction of solid-liquid interfacial energies $\Delta E_{SL} / A$ and solid-liquid interfacial tensions γ_{SL} that represent a free energy $\Delta G_{SL} / A$:

$$\gamma_{SL} = \frac{\Delta G_{SL}}{A} = \frac{\Delta E_{SL}}{A} - \frac{T\Delta S_{SL}}{A} \approx \frac{\Delta E_{SL}}{A} + f\frac{\Delta H_m}{A} \qquad (f \sim 0.15) \qquad (6)$$

This equation follows the definition of the solid-liquid interfacial tensions γ_{SL} as a free energy of formation of the solid-liquid interface ΔG_{SL} per surface area A. Then, we apply the definition of the free energy change ΔG_{SL} via energy changes ΔE_{SL} (here equal to enthaply due to negligible volume work) and entropy changes ΔS_{SL}, $\Delta G_{SL} = \Delta E_{SL} - T \cdot \Delta S_{SL}$. The entropy change upon formation of a solid-liquid interface from the liquid ΔS_{SL} is always smaller than the entropy of freezing ΔS_{freeze}, in which case the liquid would entirely loose mobility. The entropy of freezing ΔS_{freeze} is exactly known from experiments, following the defnition as the negative melting

enthalpy $-\Delta H_m$ divided by the melting temperatue T_m, $\Delta S_{freeze} = -\Delta H_m / T_m$.[102] The entropy loss upon forming a solid-liquid interface ΔS_{SL} is usually much lower than ΔS_{freeze}, represented by a scaling factor $f < 1$ in equation (6).

The energy difference $\Delta E_{SL} / A$ is typically calculated using a two-box or three-box method (Figure S2 in the Supplementary Information).[103] The entropy of forming the solid-liquid interface ΔS_{SL} from bulk solid and bulk water is negative as water loses some mobility near the mineral surface. The entropy contribution $-\frac{T\Delta S_{SL}}{A}$ in equation (6) is positive and its maximum value can be estimated from the melting enthalpy of ice (ΔH_m = 1.44 kcal/mol)[85] and the area density of water molecules at the interface (~10 molecules per nm^2). These assumptions yield a maximum of $\frac{\Delta H_m}{A} = +100$ mJ/m^2 if all water molecules would entirely freeze upon formation of the solid-liquid interface. The simulation of the calcium sulfate-water interfaces shows that the mobility of water at any (h k l) surface is only slightly restricted relative to the bulk water (10-20%), i.e., water remains far from being frozen. The entropy loss therefore contributes approximately $-\frac{T\Delta S}{A} \approx 0.15\frac{\Delta H_m}{A} = +15 \pm 5$ mJ/m^2 at 298.15 K:

$$\gamma_{SL} = \frac{\Delta E_{SL}}{A} + 15 \pm 5 \text{ mJ/m}^2 \qquad \text{(for Ca sulfates)} \qquad (7)$$

The solid-liquid interfacial tension is thus about +15 mJ/m^2 larger than the solid-liquid interfacial energy. This relationship was further verified by the direct computation of the mineral-water interface tension using the pressure difference method,[104, 105] which involves the time-average

vertical pressure component $p_{\perp} = p_{zz}$, the average in-plane pressure component $p_{\parallel} = \frac{p_{xx} + p_{yy}}{2}$, and the vertical extension z_0 of the simulation box in the *z* direction during molecular dynamics simulation of the interface in the NVT ensemble at equilibrium density (Figure S2a):

$$\gamma_{SL} = \frac{p_{\perp} - p_{\parallel}}{2} z_0 \quad . \tag{8}$$

This method was less practicable for all systems due to the need for long simulation times to average out fluctuations in pressure components (~20 ns simulation time for a water slab thickness of 5 nm). We selected the anhydrite (0 1 0) and reactive bassanite (0 0 1) mineral-water interfaces to apply equation (8) and obtained γ_{SL} values of +30 ±10 mJ/m^2 and –60 ±15 mJ/m^2, respectively. The equivalent γ_{SL} values from solid-liquid interfacial energies $\Delta E_{SL} / A$ (Table 5) after addition of +15 mJ/m^2 according to equation (7) are +20 ±10 mJ/m^2 γ_{SL} = –55 ±15 mJ/m^2, respectivly, demonstrating good agreement.

Another independent measurement to probe surface-solvent interactions is the heat of immersion ΔH_{imm} (Table 5).[100] ΔH_{imm} is often associated with less uncertainty than γ_{SL} derived from nucleation experiments.[41, 43, 106] Facet-average immersion energies of anhydrite were measured to be approximately 140 ± 30 mJ/m^2 and computations yield 125 ± 20 mJ/m^2.[100] Similarly, immersion energies of bassanite are reported as ~340 ± 10 mJ/m^2 from measurements and obtained as 338 ± 25 mJ/m^2 from simulations. Measurements and simulations match within the uncertainty, confirming that solid-water interfacial properties are near-quantitatively predictable. The prior laboratory measurements were performed on a series of successively dehydrated gypsum samples between 100 and 700 ºC and are associated with 5-10%

uncertainty.[100] A major cause of experimental error are changes in specific gravity during dehydration and some dependence of the heat of immersion on the different forms of bassanite (α and β forms) and anhydrite (I, II and III).[1] Computation of the immersion energy involved three simulation boxes (Figure S2 in the Supplementary Information).

Table 5. Solid-water interfacial energy for (h k l) surfaces, heat of immersion, and solid-liquid interfacial tension γ_{SL} of calcium sulfate minerals in pure water under ambient conditions according to molecular dynamics simulations and available experimental data. Values match within the uncertainty where experimental data are available.

Mineral	Solid-water interfacial energy $\Delta E_{SL}/A$ of (h k l) plane using MD (mJ/m^2)	Heat of immersion ΔH_{imm}	
		MD (mJ/m^2)	Expt (mJ/m^2)[a]
Anhydrite	5 ± 9 (0 1 0) 62 ± 20 (1 0 0) 110 ± 15 (0 0 1)	Facet average:[b] 125 ± 20	Facet average: ~140 ± 30
Bassanite	–70 ± 15 (0 0 1) 12 ± 5 (0 1 0) 97 ± 15 (1 0 0)	Facet average:[b] 338 ± 25	Facet average: ~340 ± 10
Gypsum	63 ± 10 (0 1 0) 67 ± 5 (1 2 0), 72 ± 5 (–1 1 1) 125 ± 15 (0 1 1) Facet average:[c] 70 ± 10, 65 ± 7		

	γ_{SL} using MD (mJ/m^2)	γ_{SL} from expt (mJ/m^2)[e]
Gypsum	Facet average:[c,d] 80 ± 10	Facet average: 76 ± 20

[a] Ref. [100]. [b] An arithmetic facet-average is reported because (hkl) surface energies are similar in vacuum. [c] An equibrium facet-average is assumed in solution according to equations (9) and (10). [d] The relationship between interfacial tension γ_{SL} and interfacial energies $\Delta E_{SL}/A$ is

$\gamma_{SL} = \frac{\Delta E_{SL}}{A} + (15 \pm 5)$ mJ/m^2 (equation (7)). [e] Refs. [41-43].

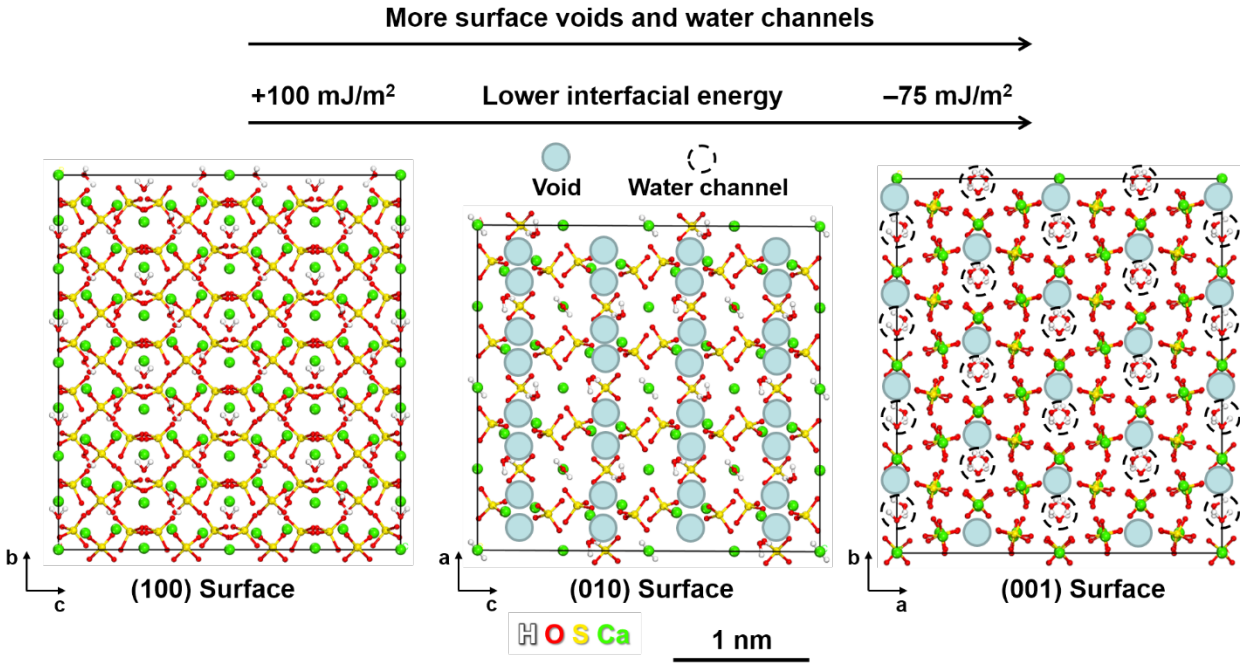

Figure 8. Top view onto the crystallographic facets of bassanite, showing the correlation of the solid-water interfacial energy with the density of surface voids and water channels (partially highlighted as filled and dashed circles). The (1 0 0) plane contains neither voids nor water channels, the (0 1 0) and (0 0 1) planes comprise numerous voids, and the (0 0 1) plane exhibits additional water channels.[101] As a result, (1 0 0) surfaces are resistant to hydration, (0 1 0) surface are hydrophilic, and (0 0 1) surfaces undergo spontaneous hydration. The models correspond to (2×4×2) super cells.

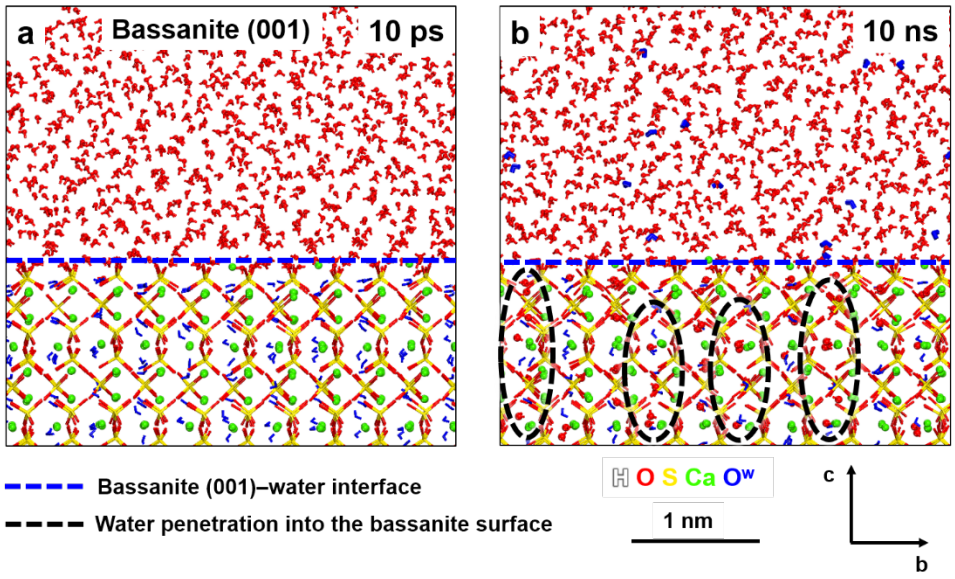

Figure 9. Exchange of water molecules on the bassanite (0 0 1) surface in contact with bulk water. Water molecules are shown in red and blue according to their origin from the liquid and solid phases, respectively (hydrogen atoms not shown for clarity). (a) Molecular dynamics snapshot before exchange at 10 ps simulation time. (b) Molecular dynamics snapshot during the exchange after 10 ns simulation time. The dissociation of blue water molecules from the mineral into the solution phase and the intrusion of red water molecules from solution into the mineral (black highlights) can be seen.

4.3. Equilibrium Crystal Shape

The equilibrium crystal shape is essential to determine (h k l) surface-average properties. Little is known from experiment about the equilibrium shape of anhydrite and basanite, however, the shape of gypsum crystals has been studied upon nucleation in solution and theoretically via calculations of lattice energies (Figure 7).[50, 92, 94, 96, 98, 107] Usually at least some interfacial water is

present in experimental studies so that models in solution are more common. The data indicate that at least 70% of surface area of gypsum crystals in solution consists of (0 1 0) facets, and the overall surface free energy γ_{cryst} of a typical gypsum crystal may be composed as follows:[50, 92, 94, 96, 98, 107]

$$\gamma_{cryst} = 0.75\gamma_{010} + 0.15\gamma_{120} + 0.10\gamma_{011} \quad (9)$$

$$\gamma_{cryst} = 0.75\gamma_{010} + 0.15\gamma_{120} + 0.10\gamma_{-111} \quad (10)$$

The uncertainty in percentage contribution of each surface is approximately ±5% due to possible differences in the local environment and, as an approximation, we assume here the same equilibrium morphology of gypsum crystals in solution and in vacuum.[55] The origin of the ratios corresponds to the interpretation of the habit of gypsum crystals grown from aqueous solution (Figure 7a)[98] and the typical (0 1 0), (1 2 0), and (–1 1 1) crystal facets observed in experiment (Figure 7b).[50] Other facets and different facet combinations were also observed in natural gypsum crystals and may play a role in crystal growth and for organic-inorganic interfaces (Figure 7c). Equations (9) and (10) yield closely the same results as the surface energies of (0 1 1) and (–1 1 1) facets are similar.

The average surface energy of gypsum crystals in vacuum according to molecular simulation and equations (9) and (10) is 348 ± 15 mJ/m^2, which agrees with facet-average measurements of 365 ± 25 mJ/m^2 (Table 4).[38-40] The expected equilibrium crystal shape for the calcium sulfate phases can also be constructed from simulation results using a broad set of (h k l) interfacial energies and the Wulff algorithm.[108, 109] For example, gypsum features a much lower cleavage energy of (0 1 0) surfaces versus other (h k l) surfaces (Table 4) that lets expect a stronger contribution of (0 1

0) planes to the crystal shape in air than in equations (9) and (10), whereas more similar (h k l) solid-liquid interfacial energies (Table 5) let expect a modest preference for (0 1 0) and (0 2 0) surfaces and more contributions by other (h k l) facets in solution.

Further validation of mechanical properties and thermal expansion is described in a follow-on paper (see summaries in Tables S2 and S3 in the Supplementary Information), as well as new insights into dehydration reactions and organic interactions.[71]

5. Conclusions

We introduced an all-atom force field for the calcium sulfate minerals anhydrite ($CaSO_4$), bassanite ($CaSO_4 \cdot 0.5\ H_2O$), and gypsum ($CaSO_4 \cdot 2H_2O$) using a single set of parameters. The parameters add to the Interface force field (IFF) and follow a rigorous validation scheme, featuring mobility of all atoms, computed structural, energetic, mechanical, and thermal properties in excellent agreement with experiment, as well as compatibility with common polynomial force fields (PCFF, AMBER, CHARMM, CVFF, DREIDING, GROMACS, OPLS-AA). The reliability is several times higher than in other force fields such as ReaxFF and ClayFF, which involve large inconsistencies, as well as in DFT calculations.

Specifically, the lattice parameters of all minerals are computed with average deviations <1% from X-ray data. Cleavage energies, heats of immersion, solid-liquid interfacial energies, elastic moduli, and thermal expansion coefficients (Tables S2 and S3)[71] match available experimental data within their uncertainty (about ±5%), and key features of vibrational spectra are reproduced. The force field eliminates large inconsistencies up to 100% in earlier models. The models are extensible to other sulfates, mixed mineral phases and sulfonates.

We obtained insight into unknown (h k l) cleavage and hydration properties that explain available measurements at the atomic scale. Anhydrite ($CaSO_4$) exhibits rather isotropic specific surface energies with equivalent (0 4 0) and (1 0 0) planes of 540 mJ/m^2 energy, followed by (0 0 1) planes with 600 mJ/m^2 energy. The inclusion of crystal water reduces the surface energy to about 380 mJ/m^2 for the (0 0 1) plane in hemihydrate (bassanite, $CaSO_4 \cdot 0.5H_2O$) while high energy planes above 600 mJ/m^2 remain present. Continued hydration to gypsum ($CaSO_4 \cdot 2H_2O$) leads to the dominant (0 1 0) cleavage plane of 270 mJ/m^2 surface energy, and still several (h k l) facets with energies between 500 and 600 mJ/m^2 are found.

The (h k l) solid-water interfacial energies were also found to be anisotropic, and exhibit different anisotropies in comparison to the corresponding (h k l) cleavage energies in vacuum. The (h k l) interfacial energies with water allow interesting correlations with solubility. Low solid-water interfacial energies (or interfacial free energies) indicate better solubility, for example, a negative value for the bassanite (001) surface of –70 mJ/m^2 equates to spontaneous dissolution. Moderately positive solid-water interfacial energies for anhydrite and gypsum correspond to decreased solubility. The results overall indicate quite anisotropic patterns of dissolution and crystal growth that are now predictable and could be interesting subjects of further investigation.

Follow-on studies also show predictions of phase equilibria and (hkl) differential interactions of calcium sulfates with organic additives in unprecedented accuracy (see separate ref. [71]). The force field and surface models can be applied to sulfate phases, electrolyte solutions, and interfacial interactions with minerals, metals, and polymers to computationally support the design of building materials, functional nanomaterials, and medicinal applications. The parameters are extensible to similar sulfur compounds by chemical analogy. The exceptionally broad validation adds to a series

of quantitative models for phosphates, clays, silica, cement minerals, metals, 2D materials, and other compounds in IFF and provides a path to expand high-level electronic structure methods to the large nanoscale. Reliable, interpretable, and compatible interatomic potentials are also suitable for large-scale computational screening and accelerated property predictions by machine learning.

Supplementary Information Available: Further details of crystal structures of calcium sulfates, computational methods, molecular models of unit cells and (h k l) surfaces, and force field parameter files.

Author Contributions: H. H. conceived the study. H. H., R. K. M., K. K., and J. J. W. designed the computational protocol and carried out the simulations. R. K. M., R. J. F., and H. H. contributed to the analysis and discussion of the results. All authors wrote the manuscript.

Acknowledgements

The authors acknowledge support by the ETH Zurich Foundation, Sika Technology AG, the National Science Foundation (DMREF 1623947, CBET 1530790, OAC 1931587, CMMI 1940335), the Swiss Commission for Technological Innovation (KTI 15846.1 PFIW-IW), the Swiss Competence Center for Energy Research – Supply of Electricity (SCCER-SoE), the University of Akron and the University of Colorado Boulder. The allocation of computational resources at the ETH Zurich, at the Ohio Supercomputing Center, and at the Janus Supercomputer at the University of Colorado-Boulder (NSF CNS-0821794) is also acknowledged.

References

[1] F. Wirsching, Calcium Sulfate, Ullmann's Encyclopedia of Industrial Chemistry2000.
[2] A.E.S. Van Driessche, T.M. Stawski, L.G. Benning, M. Kellermeier, Calcium Sulfate Precipitation Throughout Its Phase Diagram, in: A.E.S. Van Driessche, M. Kellermeier, L.G. Benning, D. Gebauer (Eds.) New Perspectives on Mineral Nucleation and Growth, Springer, Switzerland, 2017.
[3] C.L. Nelson, S.G. McLaren, R.A. Skinner, M.S. Smeltzer, J.R. Thomas, K.M. Olsen, The treatment of experimental osteomyelitis by surgical debridement and the implantation of calcium sulfate tobramycin pellets, Journal of Orthopaedic Research, 20 (2002) 643-647.
[4] F.P. Glasser, L. Zhang, High-performance cement matrices based on calcium sulfoaluminate–belite compositions, Cement and Concrete Research, 31 (2001) 1881-1886.
[5] M.M. Mbogoro, M.E. Snowden, M.A. Edwards, M. Peruffo, P.R. Unwin, Intrinsic Kinetics of Gypsum and Calcium Sulfate Anhydrite Dissolution: Surface Selective Studies under Hydrodynamic Control and the Effect of Additives, The Journal of Physical Chemistry C, 115 (2011) 10147-10154.
[6] H. Weiss, M.F. Bräu, How Much Water Does Calcined Gypsum Contain?, Angewandte Chemie International Edition, 48 (2009) 3520-3524.
[7] R.K. Mishra, L. Fernandez-Carrasco, R.J. Flatt, H. Heinz, A force field for tricalcium aluminate to characterize surface properties, initial hydration, and organically modified interfaces in atomic resolution, Dalton Transactions, 43 (2014) 10602-10616.
[8] H.F.W. Taylor, Cement Chemistry, Academic Press, London1997.
[9] C.M. Kelly, R.M. Wilkins, S. Gitelis, C. Hartjen, J.T. Watson, P.T. Kim, The Use of a Surgical Grade Calcium Sulfate as a Bone Graft Substitute: Results of a Multicenter Trial, Clin. Orthop. Rel. Res., 382 (2001) 42-50.
[10] S.L. Bahn, Plaster: A Bone Substitute, Oral Surgery, Oral Medicine, Oral Pathology, 21 (1966) 672-681.
[11] M.V. Thomas, D.A. Puleo, Calcium Sulfate: Properties and Clinical Applications, J. Biomedical Mater. Res. B: Applied Biomater., 88B (2009) 597-610.
[12] A. Liakopoulos, A. Katerinopoulos, T. Markopoulos, J. Boulegue, A Mineralogical Petrographic and Geochemical Study of Samples from Wells in the Geothermal Field of Milos Island (Greece), Geothermics, 20 (1991) 237-256.
[13] R.J. Flatt, F. Caruso, A.M.A. Sanchez, G.W. Scherer, Chemo-mechanics of salt damage in stone, Nat Commun, 5 (2014).
[14] I. Sass, U. Burbaum, Damage to the historic town of Staufen (Germany) caused by geothermal drillings through anhydrite-bearing formations, Acta Carsologica, 39 (2010).
[15] D. Feldman, D. Banu, D. Hawes, E. Ghanbari, Obtaining an energy storing building material by direct incorporation of an organic phase change material in gypsum wallboard, Solar energy materials, 22 (1991) 231-242.
[16] T.Z. Lin, H. Heinz, Accurate Force Field Parameters and pH Resolved Surface Models for Hydroxyapatite to Understand Structure, Mechanics, Hydration, and Biological Interfaces, J. Phys. Chem. C, 120 (2016) 4975-4992.
[17] H. Heinz, H. Ramezani-Dakhel, Simulations of Inorganic–Bioorganic Interfaces to Discover New Materials: Insights, Comparisons to Experiment, Challenges, and Opportunities, Chem. Soc. Rev., 45 (2016) 412-448.
[18] R.K. Mishra, L. Fernández-Carrasco, R.J. Flatt, H. Heinz, A Force Field for Tricalcium Aluminate to Characterize Surface Properties, Initial Hydration, and Organically Modified Interfaces in Atomic Resolution, Dalton Trans., 43 (2014) 10602-10616.

[19] R.K. Mishra, R.J. Flatt, H. Heinz, Force Field for Tricalcium Silicate and Insight into Nanoscale Properties: Cleavage, Initial Hydration, and Adsorption of Organic Molecules, J. Phys. Chem. C, 117 (2013) 10417-10432.
[20] H. Heinz, T.-J. Lin, R.K. Mishra, F.S. Emami, Thermodynamically Consistent Force Fields for the Assembly of Inorganic, Organic, and Biological Nanostructures: The INTERFACE Force Field, Langmuir, 29 (2013) 1754-1765.
[21] A.E. Charola, J. Pühringer, M. Steiger, Gypsum: A Review of its Role in the Deterioration of Building Materials, Environ Geol, 52 (2007) 339-352.
[22] A. Saha, J. Lee, S.M. Pancera, M.F. Bräeu, A. Kempter, A. Tripathi, A. Bose, New Insights into the Transformation of Calcium Sulfate Hemihydrate to Gypsum Using Time-Resolved Cryogenic Transmission Electron Microscopy, Langmuir, 28 (2012) 11182-11187.
[23] Y.-W. Wang, Y.-Y. Kim, H.K. Christenson, F.C. Meldrum, A New Precipitation Pathway for Calcium Sulfate Dihydrate (Gypsum) via Amorphous and Hemihydrate Intermediates, Chem. Comm., 48 (2012) 504-506.
[24] H.T. Evans, Jr., The Thermal Expansion of Anhydrite to 1000° C, Phys. Chem. Miner., 4 (1979) 77-82.
[25] C. Bezou, A. Nonat, J.C. Mutin, A.N. Christensen, M.S. Lehmann, Investigation of the Crystal Structure of γ-$CaSO_4$, $CaSO_4 \cdot 0.5\ H_2O$, and $CaSO_4 \cdot 0.6\ H_2O$ by Powder Diffraction Methods, Journal of Solid State Chemistry, 117 (1995) 165-176.
[26] F.C. Hawthorne, R.B. Ferguson, Anhydrous sulphates; II, Refinement of the crystal structure of anhydrite, The Canadian Mineralogist, 13 (1975) 289-292.
[27] B.F. Pedersen, D. Semmingsen, Neutron diffraction refinement of the structure of gypsum, $CaSO_4 . 2H_2O$, Acta Crystallographica Section B, 38 (1982) 1074-1077.
[28] W. Schwerdtner, J.-M. Tou, P. Hertz, Elastic properties of single crystals of anhydrite, Canadian Journal of Earth Sciences, 2 (1965) 673-683.
[29] A. Stark, Seismic Methods and Applications: a Guide for the Detection of Geologic Structures, Earthquake Zones and Hazards, Resource Exploration, and Geotechnical Engineering, Universal-Publishers2010.
[30] H. Voigtländer, B. Winkler, W. Depmeier, K. Knorr, L. Ehm, Host–Guest Interactions in Bassanite, CaSO4·0.5 H2O, Host-Guest-Systems Based on Nanoporous Crystals, Wiley-VCH Verlag GmbH & Co. KGaA2005, pp. 280-305.
[31] E.C. Robertson, R.A. Robie, K.G. Books, Physical properties of salt, anhydrite and gypsum : preliminary report, Trace Elements MemorandumUSGS Publications Warehouse, USA, 1958, pp. 38.
[32] N. Brantut, A. Schubnel, E.C. David, E. Héripré, Y. Guéguen, A. Dimanov, Dehydration-induced damage and deformation in gypsum and implications for subduction zone processes, Journal of Geophysical Research: Solid Earth, 117 (2012) 1-17.
[33] H. Evans, Jr., The thermal expansion of anhydrite to 1000° C, Phys Chem Minerals, 4 (1979) 77-82.
[34] P. Ballirano, E. Melis, Thermal behaviour of β-anhydrite $CaSO_4$ to 1,263 K, Phys Chem Minerals, 34 (2007) 699-704.
[35] P. Ballirano, E. Melis, Thermal behaviour and kinetics of dehydration of gypsum in air from in situ real-time laboratory parallel-beam X-ray powder diffraction, Phys Chem Minerals, 36 (2009) 391-402.
[36] P. Ballirano, E. Melis, Thermal behaviour and kinetics of dehydration in air of bassanite, calcium sulphate hemihydrate ($CaSO_4 \cdot 0.5\ H_2O$), from X-ray powder diffraction, European Journal of Mineralogy, 21 (2009) 985-993.

[37] P.F. Schofield, K.S. Knight, Thermal expansion of gypsum investigated by neutron powder diffraction, American Mineralogist, 81 (1996) 847-851.
[38] M.L. Oglesby, P.L. Gutshall, J.M. Phillips, Cleavage surface energy of selenite, American Mineralogist, 61 (1976) 295-298.
[39] O. Kimura, A Method for Measuring the Surface Energy of Solid, Bulletin of the Chemical Society of Japan, 17 (1942) 61-63.
[40] M.L. Dundon, E. Mack, The solubility and surface energy of calcium sulfate, Journal of the American Chemical Society, 45 (1923) 2479-2485.
[41] A.E. Nielsen, O. Söhnel, Interfacial tensions electrolyte crystal-aqueous solution, from nucleation data, Journal of Crystal Growth, 11 (1971) 233-242.
[42] O. Söhnel, Electrolyte crystal-aqueous solution interfacial tensions from crystallization data, Journal of Crystal Growth, 57 (1982) 101-108.
[43] M. Prisciandaro, E. Olivieri, A. Lancia, D. Musmarra, PBTC as an Antiscalant for Gypsum Precipitation: Interfacial Tension and Activation Energy Estimation, Industrial & Engineering Chemistry Research, 51 (2012) 12844-12851.
[44] A.S. Bhalla, W.R. Cook, R.F.S. Hearmon, J. Jerphagnon, S.K. Kurtz, S.T. Liu, D.F. Nelson, J.L. Oudar, Crystal and solid state physics, elastic, piezoelectric, pyroelectric, piezooptic, electrooptic constants, and nonlinear dielectric susceptibilities of crystals, Crystal Research and Technology, 19 (1984) 1404-1404.
[45] M.D. Lane, Mid-infrared emission spectroscopy of sulfate and sulfate-bearing minerals, American Mineralogist, 92 (2007) 1-18.
[46] D.F. Blake, R.V. Morris, G. Kocurek, S. Morrison, R. Downs, D. Bish, D. Ming, K. Edgett, D. Rubin, W. Goetz, Curiosity at Gale Crater, Mars: Characterization and Analysis of the Rocknest Sand Shadow, Science, 341 (2013) 1239505.
[47] N.B. Singh, B. Middendorf, Calcium sulphate hemihydrate hydration leading to gypsum crystallization, Progress in Crystal Growth and Characterization of Materials, 53 (2007) 57-77.
[48] H. Shindo, A. Seo, T. Watabe, Structures of the $CaSO_4$(001) surface studied with atomic force microscopy in air and in solution, Physical Chemistry Chemical Physics, 3 (2001) 230-234.
[49] J. Morales, J.M. Astilleros, L. Fernández-Díaz, Letter. A nanoscopic approach to the kinetics of anhydrite (100) surface growth in the range of temperatures between 60 and 120° C, American Mineralogist, 97 (2012) 995-998.
[50] W.M.M. Heijnen, P. Hartman, Structural morphology of gypsum ($CaSO_4 \cdot 2H_2O$), brushite ($CaHPO_4 \cdot 2H_2O$) and pharmacolite ($CaHAsO_4 \cdot 2H_2O$), Journal of Crystal Growth, 108 (1991) 290-300.
[51] H. Heinz, U.W. Suter, Atomic Charges for Classical Simulations of Polar Systems, The Journal of Physical Chemistry B, 108 (2004) 18341-18352.
[52] J. Chen, E. Zhu, J. Liu, S. Zhang, Z. Lin, X. Duan, H. Heinz, Y. Huang, J.J.D. Yoreo, Building Two-Dimensional Materials One Row at a Time: Avoiding the Nucleation Barrier, Science, 362 (2018) 1135-1139.
[53] C. Pramanik, J.R. Gissinger, S. Kumar, H. Heinz, Carbon Nanotube Dispersion in Solvents and Polymer Solutions: Mechanisms, Assembly, and Preferences, ACS Nano, 11 (2017) 12805-12816.
[54] H. Ramezani-Dakhel, P.A. Mirau, R.R. Naik, M.R. Knecht, H. Heinz, Stability, Surface Features, and Atom Leaching of Palladium Nanoparticles: Toward Prediction of Catalytic Functionality, Phys. Chem. Chem. Phys., 15 (2013) 5488-5492.
[55] J.-R. Hill, J. Plank, Retardation of setting of plaster of Paris by organic acids: Understanding the mechanism through molecular modeling, Journal of Computational Chemistry, 25 (2004) 1438-1448.

[56] W. Shi, M. Xia, W. Lei, F. Wang, Molecular Dynamics Study of Polyether Polyamino Methylene Phosphonates as an Inhibitor of Anhydrite Crystal, Desalination, 322 (2013) 137-143.
[57] P. Jouanna, L. Pèdesseau, G. Pèpe, D. Mainprice, Mass and momentum interface equilibrium by molecular modeling. Simulating AFM adhesion between (120) gypsum faces in a saturated solution and consequences on gypsum cohesion, Cement and Concrete Research, 38 (2008) 290-299.
[58] C.D. Adam, Atomistic modelling of the hydration of CaSO4, Journal of Solid State Chemistry, 174 (2003) 141-151.
[59] Materials Studio 6.0, Cerius2, and Discover programs, Accelrys Inc., San Diego, CA, (2011).
[60] CHARMM Developer Website (CHARMM36 and above), http://www.charmm.org/package/releases.html.
[61] A.D. MacKerell, Jr., D. Bashford, M. Bellott, R.L. Dunbrack, Jr., J.D. Evanseck, M.J. Fields, S. Fischer, J. Gao, H. Guo, S. Ha, D. Joseph-McCarthy, L. Kuchnir, K. Kuczera, F.T.K. Lau, C. Mattos, S. Michnick, T. Ngo, D.T. Nguyen, B. Prodhom, W.E. Reiher, III, B. Roux, M. Schlenkrich, J.C. Smith, R. Stote, J. Straub, D. Watanabe, J. Wiórkiewicz-Kuczera, D. Yin, M. Karplus, All-Atom Empirical Potential for Molecular Modeling and Dynamics Studies of Proteins, J. Phys. Chem. B, 102 (1998) 3586-3616.
[62] W.L. Jorgensen, D.S. Maxwell, J. TiradoRives, Development and Testing of the OPLS All-Atom Force Field on Conformational Energetics and Properties of Organic Liquids, J. Am. Chem. Soc., 118 (1996) 11225-11236.
[63] D. Kony, W. Damm, S. Stoll, W.F. Van Gunsteren, An Improved OPLS-AA Force Field for Carbohydrates, J. Comput. Chem., 23 (2002) 1416-1429.
[64] J.M. Wang, R.M. Wolf, J.W. Caldwell, P.A. Kollman, D.A. Case, Development and Testing of a General Amber Force Field, J. Comput. Chem., 25 (2004) 1157-1174.
[65] H. Heinz, U.W. Suter, Atomic Charges for Classical Simulations of Polar Systems, J. Phys. Chem. B, 108 (2004) 18341-18352.
[66] V.G. Ruiz, W. Liu, A. Tkatchenko, Density-Functional Theory with Screened van der Waals Interactions Applied to Atomic and Molecular Adsorbates on Close-Packed and Non-Close-Packed Surfaces, Phys. Rev. B, 93 (2016) 035118.
[67] P.L. Silvestrelli, A. Ambrosetti, Van Der Waals Corrected Density Functional Theory Simulation of Adsorption Processes on Noble-Metal Surfaces: Xe on Ag(111), Au(111), and Cu(111), J. Low Temp. Phys., 185 (2016) 183-197.
[68] M. Khalkhali, X.M. Ma, H. Zhang, Q.X. Liu, Bulk and Surface Properties of Gypsum: A Comparison between Classical Force Fields and Dispersion-Corrected DFT Calculations, Comput. Mater. Sci., 164 (2019) 8-16.
[69] F.S. Emami, V. Puddu, R.J. Berry, V. Varshney, S.V. Patwardhan, C.C. Perry, H. Heinz, Force Field and a Surface Model Database for Silica to Simulate Interfacial Properties in Atomic Resolution, Chemistry of Materials, 26 (2014) 2647-2658.
[70] R.K. Mishra, A.K. Mohamed, D. Geissbühler, H. Manzano, T. Jamil, R. Shahsavari, A.G. Kalinichev, S. Galmarini, L. Tao, H. Heinz, R. Pellenq, A.C.T. van Duin, S.C. Parker, R.J. Flatt, P. Bowen, Cemff: A Force Field Database for Cementitious Materials Including Validations, Applications and Opportunities, Cem. Concr. Res., 102 (2017) 68-89.
[71] R.K. Mishra, R.J. Flatt, H. Heinz, Understanding Phase Equilibria, Mechanical Properties, Thermal Expansion, and Organic Interfacial Interactions of Calcium Sulfate Hydrates from the Atomic Scale, (2020) (submitted).

[72] G.M. Psofogiannakis, J.F. McCleerey, E. Jaramillo, A.C.T. van Duin, ReaxFF Reactive Molecular Dynamics Simulation of the Hydration of Cu-SSZ-13 Zeolite and the Formation of Cu Dimers, J. Phys. Chem. C, 119 (2015) 6678-6686.
[73] R.A. Robie, S. Russell-Robinson, B.S. Hemingway, Heat capacities and entropies from 8 to 1000 K of langbeinite ($K_2Mg_2(SO_4)_3$), anhydrite ($CaSO_4$) and of gypsum ($CaSO_4{\cdot}2H_2O$) to 325 K, Thermochim. Acta, 139 (1989) 67-81.
[74] S. Haussühl, Elastische und thermoelastische Eigenschaften von $CaSO_4 \cdot 2H_2O$ (Gips), Zeitschrift für Kristallographie, 122 (1965) 311-314.
[75] J.-P. Boisvert, M. Domenech, A. Foissy, J. Persello, J.-C. Mutin, Hydration of calcium sulfate hemihydrate ($CaSO_4{\cdot}12H_2O$) into gypsum ($CaSO_4{\cdot}2H_2O$). The influence of the sodium poly(acrylate)/surface interaction and molecular weight, Journal of Crystal Growth, 220 (2000) 579-591.
[76] Y. Yun, D. Legut, P.M. Oppeneer, Phonon Spectrum, Thermal Expansion and Heat Capacity of UO_2 from First-Principles, J. Nucl. Mater., 426 (2012) 109-114.
[77] J. Wang, R.M. Wolf, J.W. Caldwell, P.A. Kollman, D.A. Case, Development and Testing of a General Amber Force Field, J. Comput. Chem., 25 (2004) 1157-1174.
[78] P. Dauber-Osguthorpe, V.A. Roberts, D.J. Osguthorpe, J. Wolff, M. Genest, A.T. Hagler, Structure and energetics of ligand binding to proteins: Escherichia coli dihydrofolate reductase-trimethoprim, a drug-receptor system, Proteins: Structure, Function, and Bioinformatics, 4 (1988) 31-47.
[79] W.L. Jorgensen, D.S. Maxwell, J. Tirado-Rives, Development and Testing of the OPLS All-Atom Force Field on Conformational Energetics and Properties of Organic Liquids, Journal of the American Chemical Society, 118 (1996) 11225-11236.
[80] R.K. Mishra, R.J. Flatt, H. Heinz, Force Field for Tricalcium Silicate and Insight into Nanoscale Properties: Cleavage, Initial Hydration, and Adsorption of Organic Molecules, The Journal of Physical Chemistry C, 117 (2013) 10417-10432.
[81] H. Heinz, H. Koerner, K.L. Anderson, R.A. Vaia, B.L. Farmer, Force Field for Mica-Type Silicates and Dynamics of Octadecylammonium Chains Grafted to Montmorillonite, Chem. Mater., 17 (2005) 5658-5669.
[82] A. Kirfel, G. Will, Charge density in anhydrite, CaSO4, from X-ray and neutron diffraction measurements, Acta Crystallographica Section B, 36 (1980) 2881-2890.
[83] E. Pustovgar, R.K. Mishra, M. Palacios, J.-B. d'Espinose de Lacaillerie, T. Matschei, A.S. Andreev, H. Heinz, R. Verel, R.J. Flatt, Influence of aluminates on the hydration kinetics of tricalcium silicate, Cement and Concrete Research, 100 (2017) 245-262.
[84] J. Liu, E. Tennessen, J. Miao, Y. Huang, J.M. Rondinelli, H. Heinz, Understanding Chemical Bonding in Alloys and the Representation in Atomistic Simulations, J. Phys. Chem. C, 122 (2018) 14996-15009.
[85] CRC Handbook of Chemistry and Physics, 101st ed., CRC Press, Boca Raton, FL, 2020.
[86] S.S. Batsanov, Van der Waals radii of elements, Inorg. Mater., 37 (2001) 871-885.
[87] Y. Liu, A. Wang, J. Freemen, Raman, MIR, and NIR spectroscopic study of calcium sulfates: gypsum, bassanite, and anhydrite, Lunar and Planetary Science Conference, 2009, pp. 2128.
[88] B. Lafuente, R. Downs, H. Yang, N. Stone, The power of databases: the RRUFF project, Highlights in Mineralogical Crystallography, ed. T. Armbruster and RM Danisi, W. De Gruyter, Berlin, Germany, (2015) 1-30.
[89] W.L. Jorgensen, J. Tirado-Rives, Potential Energy Functions for Atomic-Level Simulations of Water and Organic and Biomolecular Systems, Proc. Natl. Acad. Sci. U. S. A., 102 (2005) 6665-6670.

[90] H. Heinz, R.A. Vaia, B.L. Farmer, Interaction Energy and Surface Reconstruction Between Sheets of Layered Silicates, J. Chem. Phys., 124 (2006) 224713.
[91] Y.T. Fu, H. Heinz, Cleavage Energy of Alkylammonium-Modified Montmorillonite and Relation to Exfoliation in Nanocomposites: Influence of Cation Density, Head Group Structure, and Chain Length, Chem. Mater., 22 (2010) 1595-1605.
[92] B. Simon, M. Bienfait, Structure et mécanisme de croissance du gypse, Acta Crystallographica, 19 (1965) 750-756.
[93] M.P.C. Weijnen, G.M. van Rosmalen, P. Bennema, J.J.M. Rijpkema, The adsorption of additives at the gypsum crystal surface: A theoretical approach, Journal of Crystal Growth, 82 (1987) 509-527.
[94] I.N. Stranski, Propriétés des surfaces des cristaux, Bull. Soc. Fr. Minér. Crist, 79 (1956) 359-382.
[95] P. Niggli, Tabellen zur Allgemeinen und Speziellen Mineralogie, Gebrüder Borntraeger1927.
[96] H. Bartels, H. Follner, Crystal growth and twin formation of gypsum), Crystal Research and Technology, 24 (1989) 1191-1196.
[97] H. Heinz, R.A. Vaia, B.L. Farmer, R.R. Naik, Accurate Simulation of Surfaces and Interfaces of Face-Centered Cubic Metals Using 12−6 and 9−6 Lennard-Jones Potentials, J. Phys. Chem. C, 112 (2008) 17281-17290.
[98] E. van der Voort, P. Hartman, The habit of gypsum and solvent interaction, Journal of Crystal Growth, 112 (1991) 445-450.
[99] A.R. Roosen, R.P. McCormack, W.C. Carter, Wulffman: A tool for the calculation and display of crystal shapes, Computational materials science, 11 (1998) 16-26.
[100] S. Gregg, E. Willing, 648. The dehydration of gypsum. Part IV. The heat of immersion, heat of hydration, specific gravity, sedimentation volume, and bulk density of the dehydration products, Journal of the Chemical Society (Resumed), (1951) 2921-2924.
[101] H. Schmidt, I. Paschke, D. Freyer, W. Voigt, Water channel structure of bassanite at high air humidity: crystal structure of $CaSO_4 \cdot 0.625H_2O$, Acta Crystallographica Section B, 67 (2011) 467-475.
[102] D.A. McQuarrie, J.D. Simon, Physical Chemistry – A Molecular Approach, University Science Books, Sausalito, CA, 1997.
[103] H. Heinz, Computational Screening of Biomolecular Adsorption and Self-Assembly on Nanoscale Surfaces, J. Comput. Chem., 31 (2010) 1564-1568.
[104] J.O. Hirschfelder, C.F. Curtiss, R.B. Bird, Molecular Theory of Gases and Liquids, John Wiley, New York, 1954.
[105] H. Heinz, Calculation of Local and Average Pressure Tensors in Molecular Simulations, Mol. Sim., 33 (2007) 747-758.
[106] O. Söhnel, Electrolyte Crystal-Aqueous Solution Interfacial Tensions from Crystallization Data, J. Cryst. Growth, 57 (1982) 101-108.
[107] M.P.C. Weijnen, G.M. van Rosmalen, P. Bennema, J.J.M. Rijpkema, The Adsorption of Additives at the Gypsum Crystal Surface: A Theoretical Approach, J. Cryst. Growth, 82 (1987) 509-527.
[108] E. Ringe, R.P. Van Duyne, L.D. Marks, Kinetic and Thermodynamic Modified Wulff Constructions for Twinned Nanoparticles, J. Phys. Chem. C, 117 (2013) 15859-15870.
[109] A.R. Roosen, R.P. McCormack, W.C. Carter, Wulffman: A Tool for the Calculation and Display of Crystal Shapes, Comput. Mater. Sci., 11 (1998) 16-26.